Emission of photon pairs by mechanical stimulation of the squeezed vacuum

Wei Qin,[1] Vincenzo Macrì,[1] Adam Miranowicz,[1,2] Salvatore Savasta,[1,3] and Franco Nori[1,4]

[1]*Theoretical Quantum Physics Laboratory, RIKEN Cluster for Pioneering Research, Wako-shi, Saitama 351-0198, Japan*

[2]*Faculty of Physics, Adam Mickiewicz University, 61-614 Poznań, Poland*

[3]*Dipartimento di Scienze Matematiche e Informatiche, Scienze Fisiche e Scienze della Terra, Università di Messina, I-98166 Messina, Italy*

[4]*Department of Physics, The University of Michigan, Ann Arbor, Michigan 48109-1040, USA*

(Received 11 February 2019; revised manuscript received 4 June 2019; published 2 December 2019)

To observe the dynamical Casimir effect (DCE) induced by a moving mirror is a long-standing challenge because the mirror velocity needs to approach the speed of light. Here, we present an experimentally feasible method for observing this mechanical DCE in an optomechanical system. It employs a detuned, parametric driving to squeeze a cavity mode, so that the mechanical mode, with a typical resonance frequency, can parametrically and resonantly couple to the squeezed cavity mode, thus leading to a resonantly amplified DCE in the squeezed frame. The DCE process can be interpreted as *mechanically induced two-photon hyper-Raman scattering* in the laboratory frame. Specifically, *a photon pair* of the parametric driving absorbs a single phonon and then is scattered into an anti-Stokes sideband. We also find that the squeezing, which additionally induces and amplifies the DCE, can be extremely small. Our method requires neither an ultrahigh mechanical-oscillation frequency (i.e., a mirror moving at nearly the speed of light) nor an ultrastrong single-photon optomechanical coupling and, thus, could be implemented in a wide range of physical systems.

DOI: 10.1103/PhysRevA.100.062501

I. INTRODUCTION

One of the most astonishing phenomena of nature, predicted by quantum field theory, is that the quantum vacuum is not empty but teems with virtual particles. Under certain conditions, these vacuum fluctuations could be converted into real particles by dynamical amplification mechanisms such as the Schwinger process [1], Hawking radiation [2], and Unruh effect [3]. The dynamical Casimir effect (DCE) describes the creation of photons out of the quantum vacuum due to a moving mirror [4,5]. The physics underlying the DCE is that the electromagnetic field cannot adiabatically adapt to the time-dependent boundary condition imposed by the mechanical motion of the mirror, such that a mismatch of vacuum modes in time occurs. This gives rise to the emission of photon pairs from the vacuum and, at the same time, to the equal-energy dissipation of the mechanical phonons. Thus, according to energy conservation, the DCE can also be understood as the energy conversion of the mechanical motion to the electromagnetic field.

In order to detect the DCE, the mirror velocity is, however, required to be close to the speed of light [6,7]. This requirement is the main obstacle in observing the DCE. This problem led to many alternative proposals, which replaced the mechanical motion with an effective motion provided by, e.g., modulating dielectric properties of semiconductors or superconductors [8–12], modulating the ultrastrong light-matter coupling in cavity quantum electrodynamics (QED) [13–22], or driving an optical parametric oscillator [23]. In particular, two remarkable experimental verifications have recently been implemented utilizing a superconducting quantum interference device [7,24–28] and a Josephson metamaterial [29], respectively, to produce the effective motion. Despite such achievements, implementing the DCE with a massive mechanical mirror is still highly desirable for a more fundamental understanding of the DCE physics. This is because the parametric conversion of mechanical energy to photons, which is a key feature of the DCE predicted in its original proposals [4–7], can be demonstrated in this case, contrary to proposals based on the effective motion. However, owing to the serious problem mentioned above (i.e., very fast oscillating mirror), such a radiation has not yet been observed experimentally, although the DCE has been predicted for almost fifty years. Here, we propose an approach to this outstanding problem, and we show that in a squeezed optomechanical system, a mirror oscillating at a common frequency can induce an observable DCE.

The DCE can, in principle, also be directly implemented in cavity-optomechanical systems [30–39]. But it requires a mechanical frequency ω_m to be very close to the cavity frequency ω_c, or even a single-photon optomechanical coupling g_0 to reach the ultrastrong-coupling regime $g_0/\omega_m \gtrsim 0.1$ [36,39]. For typical parameters, $\omega_m \sim$ MHz is much smaller than $\omega_c \sim$ THz ($\sim$GHz) for optical (microwave) cavities, and at the same time, achieving the ultrastrong coupling is, currently, also a very challenging task in optomechanical experiments. However, as we describe in this paper, when squeezing the cavity [40], the squeezed-cavity-mode (SCM) frequency is tunable, such that the SCM can parametrically and resonantly couple to a mechanical mode with a typically available ω_m. This enables an observable DCE in the squeezed frame. Such a *mechanical DCE corresponds to two-photon hyper-Raman scattering* in the laboratory frame. Compared to one-photon Raman scattering typically demonstrated in

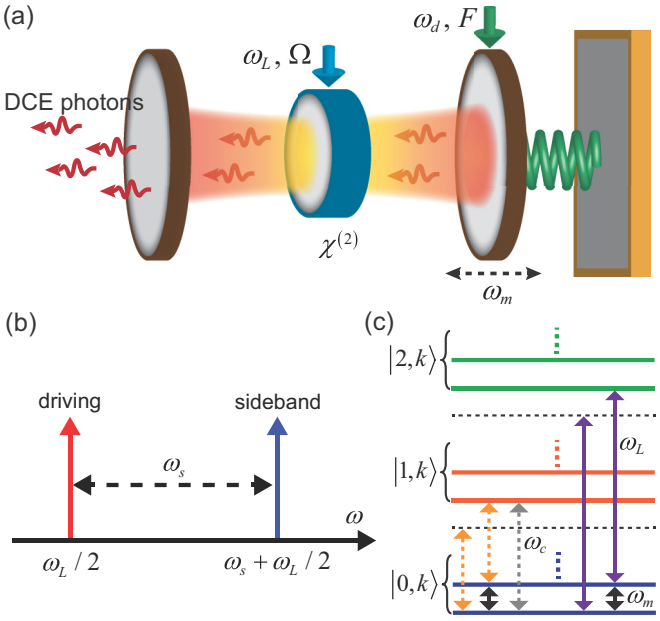

FIG. 1. (a) Setup for observing the mechanical dynamical Casimir effect. In this optomechanical system, a $\chi^{(2)}$ nonlinear crystal driven at a frequency ω_L and amplitude Ω is used to squeeze the cavity mode of frequency ω_c, and the mechanical resonator is driven by a force of frequency ω_d and amplitude F. The DCE occurs in the squeezed frame, and a large number of DCE photons, emitted from the cavity, can be observed in the laboratory frame. (b) Frequency-domain illustration of mechanically induced two-photon hyper-Raman scattering. The left arrow is the two-photon driving ($\omega_L/2$), and the right arrow is the squeezing-induced anti-Stokes sideband ($\omega_s+\omega_L/2$). The horizontal axis corresponds to the resonance frequency (ω) and the dashed double arrow to the detuning (ω_s). (c) Level diagram of the bare optomechanical system. The solid (dashed) arrows indicate two-photon hyper Raman (one-photon Raman) scattering processes induced by the optomechanical coupling. The first number in the ket refers to the photon number and the second to the phonon number k. We assume, for simplicity, that $\Omega \ll \Delta$, such that the resonance condition is $2\omega_c \approx \omega_L + \omega_m$.

cavity optomechanics, this hyper-Raman scattering process describes *a photon pair scattered into a higher energy mode by absorbing a mechanical phonon*.

As opposed to previous mechanical-DCE proposals, our approach requires *neither* an ultrahigh mechanical frequency *nor* an ultrastrong coupling. In addition, the model discussed here is a generic optomechanical setup. Hence, with current technologies our proposal could be realized in various physical architectures, e.g., superconducting resonators [41,42] and optical cavities [43]. Furthermore, our proposal also shows mechanically induced two-photon hyper-Raman scattering.

II. MODEL

We consider an optomechanical system, as schematically depicted in Fig. 1(a). The basic idea underlying our proposal is to use a detuned two-photon driving, e.g., of frequency ω_L and amplitude Ω, to squeeze the cavity mode. The driving results in parametric down conversion of mechanical phonons to correlated cavity-photon pairs, which corresponds to the DCE. Furthermore, the SCM frequency completely depends on the detuning $\Delta = \omega_c - \omega_L/2$ and the amplitude Ω. This can be exploited to tune the parametric phonon-photon coupling into resonance, determining a strong amplification of the DCE. When the mechanical mode is driven, e.g., at frequency ω_d and amplitude F, a strong steady-state output-photon flux that is induced by the DCE can be achieved.

To be specific, we consider the Hamiltonian

$$H = H_{\rm OM} + H_{\rm CD} + H_{\rm MD}. \tag{1}$$

Here,

$$H_{\rm OM} = \omega_m b^\dagger b - g_0 a^\dagger a (b + b^\dagger) \tag{2}$$

describes a standard optomechanical coupling,

$$H_{\rm CD} = \Delta a^\dagger a + \tfrac{1}{2}\Omega(a^2 + a^{\dagger 2}) \tag{3}$$

a detuned two-photon cavity driving, and

$$H_{\rm MD} = \tfrac{1}{2}F[\exp(i\omega_d t)b + \exp(-i\omega_d t)b^\dagger] \tag{4}$$

a single-phonon mechanical driving. The bare cavity mode a, when parametrically driven, is squeezed with a squeezing parameter

$$r = \frac{1}{4}\ln\left(\frac{\Delta+\Omega}{\Delta-\Omega}\right) \tag{5}$$

and accordingly is transformed to a squeezed mode a_s, via the Bogoliubov transformation [40]

$$a_s = \cosh(r)a + \sinh(r)a^\dagger. \tag{6}$$

Similar methods have been used for enhancing light-matter interactions in cavity optomechanics [44,45] and cavity QED [46,47], but involving markedly different physical processes. As a result, $H_{\rm CD}$ is diagonalized to $H_{\rm CD} = \omega_s a_s^\dagger a_s$, where $\omega_s = \sqrt{\Delta^2 - \Omega^2}$ is a controllable SCM frequency. The optomechanical-coupling Hamiltonian is transformed, in terms of a_s, to

$$H_{\rm OM} = \left[-g_{\rm OM} a_s^\dagger a_s + g_{\rm DCE}\left(a_s^2 + a_s^{\dagger 2}\right)\right](b + b^\dagger), \tag{7}$$

where $g_{\rm OM} = g_0\cosh(2r)$ is an effective single-photon optomechanical coupling, and $g_{\rm DCE} = g_0\sinh(2r)/2$ is a coupling associated with the DCE. The dynamics under $H_{\rm OM}$ describes a mechanical modulation of the boundary condition of the squeezed field [36,48,49]. Under the rotating-wave approximation, the coherent dynamics of the system is governed by an effective Hamiltonian,

$$H_{\rm eff} = \Delta_s a_s^\dagger a_s + \Delta_m b^\dagger b + g_{\rm DCE}\left(a_s^2 b^\dagger + {\rm H.c.}\right) + \tfrac{1}{2}F(b + b^\dagger), \tag{8}$$

where $\Delta_s = \omega_s - \omega_d/2$ and $\Delta_m = \omega_m - \omega_d$. We find that when $\omega_m = 2\omega_s$, the resonant DCE can be demonstrated, and that the parametric energy conversion of the mechanical motion to the electromagnetic field, which was predicted in the original DCE proposals, can therefore be observed. We also find that the energy of emitted photons in the squeezed frame completely originates from the mechanical motion. Thus, parametrically driving the cavity without a moving mirror [23], corresponding to $F = 0$, *cannot* excite the a_s mode and *cannot* result in such a parametric energy conversion from mechanics to light.

III. MECHANICALLY INDUCED TWO-PHOTON HYPER-RAMAN SCATTERING

More interestingly, the DCE in the squeezed frame can be interpreted, in the laboratory frame, as mechanically induced two-photon hyper-Raman scattering. This hyper-Raman scattering is an anti-Stokes process, as illustrated in Fig. 1(b). According to the Bogoliubov transformation, the squeezing gives rise to an anti-Stokes sideband at frequency $\omega_s + \omega_L/2$ [right arrow in Fig. 1(b)]. The two-photon driving at frequency ω_L produces photon pairs at frequency $\omega_L/2$ [left arrow in Fig. 1(b)]. When mechanical phonons at frequency $\omega_m = 2\omega_s$ are present, a driving photon pair is scattered into the anti-Stokes sideband, while simultaneously absorbing a phonon in the mechanical resonator. Because of their different frequency from the driving photon pairs, the anti-Stokes scattered photon pairs, which are referred to as the DCE photons, can be spectrally filtered from the driving photons, which are referred to as the noise photons.

In cavity optomechanics, most of the experimental and theoretical studies are carried out under detuned *one-photon* driving of a cavity, so that the cavity field can be split into an average coherent amplitude and a fluctuating term. For a red-detuned driving, a driving photon can be scattered into the cavity resonance by absorbing a phonon. This process is viewed as *mechanically induced one-photon Raman scattering* [dashed arrows in Fig. 1(c)]. As described above, our proposal instead exploits a red-detuned *two-photon* driving, and *the mechanical motion can induce two-photon hyper-Raman scattering*. In order to compare the two scattering processes more explicitly, we consider the limit $\Omega \ll \Delta$. In this limit, the a_s mode can be approximated by the a mode, i.e., $a_s \approx a$, and as a result, the anti-Stokes sideband becomes the cavity resonance. Correspondingly, the effective Hamiltonian $H_{\rm eff}$ becomes

$$\widetilde{H}_{\rm eff} = \Delta_s a^\dagger a + \omega_m b^\dagger b + g_{\rm DCE}(a^2 b^\dagger + {\rm H.c.}) + \tfrac{1}{2}F(b + b^\dagger). \quad (9)$$

Under the resonant condition $\omega_m = 2\omega_s$ (i.e., $2\omega_c \approx \omega_L + \omega_m$), the dynamics described by $\widetilde{H}_{\rm eff}$ shows that a driving photon pair, rather than a single photon, is scattered into the cavity resonance by absorbing a phonon [solid arrows in Fig. 1(c)].

IV. HOW TO OBSERVE THE DYNAMICAL CASIMIR EFFECT

In our approach, we squeeze the a mode to make the effective cavity frequency very close to the mechanical frequency. However, this squeezing also inputs thermal noise and two-photon correlation noise into the cavity. Although these undesired effects are negligible in the weak-squeezing case (see below), they can be completely eliminated by coupling a squeezed-vacuum bath, e.g., with a squeezing parameter r_e and a reference phase θ_e, to the a mode [50–54]. We assume that $r_e = r$ and $\theta_e = \pm n\pi$ $(n = 1, 3, 5, \dots)$, so that the a_s mode is equivalently coupled to a vacuum bath (see Appendix A). The full dynamics is therefore determined by

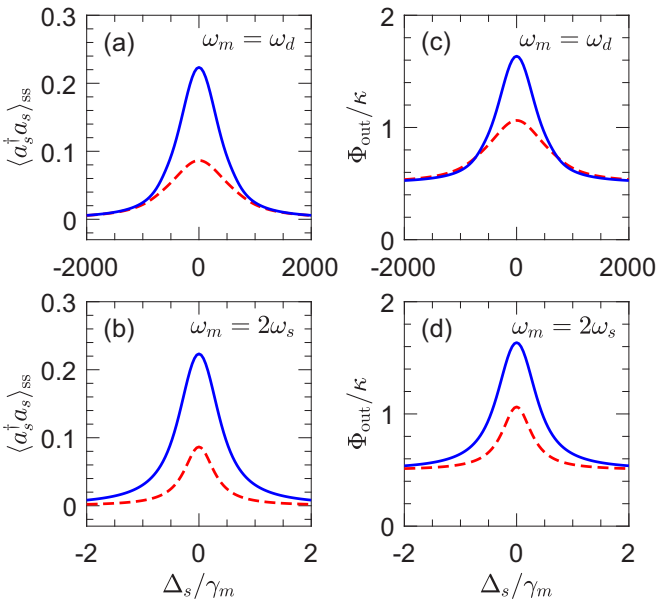

FIG. 2. (a), (b) Photon number $\langle a_s^\dagger a_s \rangle_{\rm ss}$ and (c), (d) photon flux $\Phi_{\rm out}$ versus detuning Δ_s. The emergence of the resonance peaks indicates the occurrence of the dynamical Casimir effect. We assumed $\omega_m = \omega_d$ in (a) and (c), and $\omega_m = 2\omega_s$ in (b) and (d). Solid curves correspond to $\kappa = 500\gamma_m$ and dashed curves to $\kappa = 1000\gamma_m$. In all plots, we assumed $g_0 = 10\gamma_m$, $F = 15\gamma_m$, $\omega_m = 10^4\gamma_m$, and $\sinh^2(r) = 0.5$.

the standard master equation

$$\dot{\rho}(t) = i[\rho(t), H_{\rm eff}] - \frac{\kappa}{2}\mathcal{L}(a_s)\rho(t) - \frac{\gamma_m}{2}\mathcal{L}(b)\rho(t), \quad (10)$$

where κ and γ_m are the cavity and mechanical loss rates, respectively, and we have defined

$$\mathcal{L}(o)\rho(t) = o^\dagger o\rho(t) - 2o\rho(t)o^\dagger + \rho(t)o^\dagger o. \quad (11)$$

We have also assumed that the mechanical resonator is coupled to a zero-temperature bath (see Appendix B for an analytical discussion at finite temperatures). The SCM excitation spectrum $\langle a_s^\dagger a_s \rangle_{\rm ss}(\Delta_s)$, where $\langle o \rangle_{\rm ss}$ represents a steady-state average value, is plotted in Figs. 2(a) and 2(b). Eliminating the squeezing-induced noise ensures a zero background noise for the excitation spectrum. If the mechanical resonator is driven, then photons are excited from the vacuum, and according to energy conservation, are emitted from the mechanical resonator, together with a resonance peak in the excitation spectrum.

We now return to the original laboratory frame and consider the steady-state output-photon flux. Because of the squeezing, the steady-state intracavity photon number $\langle a^\dagger a \rangle_{\rm ss}$ in the laboratory frame includes two physical contributions, i.e.,

$$\langle a^\dagger a \rangle_{\rm ss} = \Phi_{\rm BGN} + \Phi_{\rm DCE}, \quad (12)$$

where $\Phi_{\rm BGN} = \sinh^2(r)$ is the number of background-noise photons contained in the squeezed vacuum, and

$$\Phi_{\rm DCE} = \langle a_s^\dagger a_s \rangle_{\rm ss} \cosh(2r) - {\rm Re}\big[\langle a_s^2 \rangle_{\rm ss}\big] \sinh(2r) \quad (13)$$

is the number of DCE-induced photons. The output-photon flux is then given by

$$\Phi_{\rm out} = \kappa(\Phi_{\rm BGN} + \Phi_{\rm DCE}), \tag{14}$$

according to the input-output relation. We plot the flux spectrum $\Phi_{\rm out}(\Delta_s)$ in Figs. 2(c) and 2(d). There exists a nonzero background noise in the photon flux spectrum, as discussed previously. Nevertheless, when driving the mechanical resonator, the DCE-induced photons are emitted from the cavity, and a resolved resonance peak can be observed. We find that the behavior of the flux spectrum directly reflects that of the excitation spectrum. Hence, the emergence of the resonance peak in the flux spectrum can be considered as an experimentally observable signature of the DCE.

Owing to the existence of the background noise in the flux $\Phi_{\rm out}$, we now discuss the ability to resolve the DCE signal $\Phi_{\rm DCE}$ from the background noise $\Phi_{\rm BGN}$ at resonance $\omega_m = \omega_d = 2\omega_s$. In order to quantify this, we typically employ the signal-to-noise ratio, defined as

$$\mathcal{R} = \frac{\Phi_{\rm DCE}}{\Phi_{\rm BGN}}. \tag{15}$$

The signal-resolved regime often requires $\mathcal{R} > 1$, allowing for a resolved DCE-signal detection. We find that, by increasing the mechanical driving F, the signal $\Phi_{\rm DCE}$ becomes stronger, but at the same time, the noise $\Phi_{\rm BGN}$ remains unchanged. This enables an improvement in the signal-to-noise ratio with the mechanical force. Consequently, the desired signal can be directly driven from the unresolved to resolved regime, as shown in Fig. 3(a). Assuming a realistic parameter $g_0 = 10\gamma_m$, we find that a mechanical driving of $F = 15\gamma_m$ is able to keep the ratio $\mathcal{R}$ above 1 for $\kappa \leqslant 1000\gamma_m$. With these parameters, we can obtain $\langle a_s^\dagger a_s\rangle_{\rm ss} \approx 0.2$, as given in Fig. 2. Therefore, in the laboratory frame, a cavity having a typical linewidth of $\kappa/2\pi = 2.0$ MHz could emit $\approx 1.4 \times 10^7$ photons per second, which is larger than the background photon emission $\approx 6.3 \times 10^6$ per second. The ratio $\mathcal{R}$ can be made $\gg 1$ as long as the driving F is further increased, so that the background noise can be even neglected compared to the DCE signal. This is demonstrated in Appendix C, where we make a semiclassical approximation for investigating the DCE under a strong-F drive. For

$$F \gg (g_{\rm DCE} + \kappa\gamma_m/4g_{\rm DCE}), \tag{16}$$

the system behaves classically [55,56], and quantum effects are negligible. Thus in order to observe the DCE, such a regime needs to be avoided. Note, however, that the signal can still be resolved even for $\mathcal{R} < 1$, if standard techniques of Raman spectroscopy are used. This is because the background noise is due to driving photons at frequency $\omega_L/2$, while the DCE photons have a frequency $\omega_s + \omega_L/2$. The monotonic increase of the flux $\Phi_{\rm out}$ at resonance with the driving F can, therefore, be considered as another signature of the mechanical DCE in experiments.

The DCE photons are emitted in pairs, and could exhibit photon bunching [25,36,57]. The essential parameter characterizing this property is the equal-time second-order correlation function,

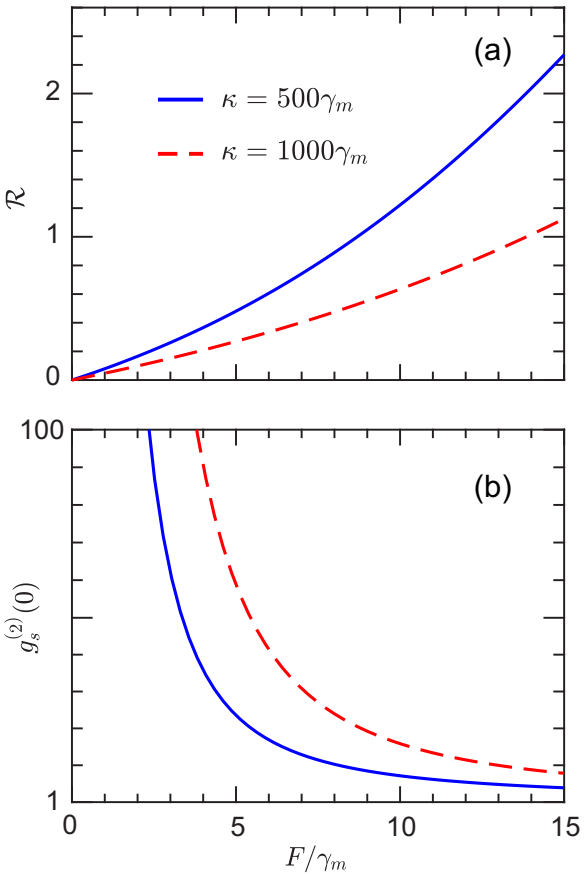

FIG. 3. (a) Signal-to-noise ratio $\mathcal{R}$ and (b) equal-time correlation $g_s^{(2)}(0)$ as a function of the mechanical driving F for $\kappa = 500\gamma_m$ and $1000\gamma_m$. Note that the signal can still be resolved even if $\mathcal{R} < 1$ with standard spectroscopic techniques used, e.g., for Raman signals. The $g_s^{(2)}(0) > 1$ correlation implies that in the squeezed frame, the photons are created in pairs from the quantum vacuum. For both plots, we assumed that $g_0 = 10\gamma_m$, $\omega_m = \omega_d = 2\omega_s$, and $\sinh^2(r) = 0.5$.

$$g_s^{(2)}(0) = \frac{\langle a_s^{\dagger 2} a_s^2\rangle_{\rm ss}}{\langle a_s^\dagger a_s\rangle_{\rm ss}^2}. \tag{17}$$

We plot it as a function of the mechanical driving in Fig. 3(b). We find that

$$g_s^{(2)}(0) \approx \frac{1}{2\langle a_s^\dagger a_s\rangle_{\rm ss}} \tag{18}$$

in the $F \to 0$ limit, and ≈ 1 in the $F \to \infty$ limit (see Appendixes B and C). Hence, for a weak-F drive, the very small $\langle a_s^\dagger a_s\rangle_{\rm ss}$ leads to $g_s^{(2)}(0) \gg 1$. This corresponds to strong photon bunching. In the special case of $F = 0$, the a_s mode cannot be excited although the two-photon driving still exists, and as a consequence, the $g_s^{(2)}(0)$ correlation cannot be observed. We also find that with increasing the driving F, the $g_s^{(2)}(0)$ correlation decreases and then, as suggested above, approaches its lower bound equal to 1. These features confirm that the photons are bunched, as required.

So far, we have assumed a model with a squeezed-vacuum bath. To avoid using such a bath and simplify the model, we

now consider the limit of $\Omega \ll \Delta$. In this limit, the effective Hamiltonian is $\tilde{H}_{\rm eff}$, as given above. In the absence of the squeezed-vacuum bath, the a mode is coupled to a vacuum bath, and the master equation is the same as given in Eq. (10), but with $a_s \mapsto a$. We find that the noise induced by squeezing the cavity, which includes thermal noise $\propto \sinh^2(r)$ and two-photon correlation noise $\propto \sinh(2r)$, becomes strongly suppressed, even when there is no squeezed-vacuum bath. The DCE dynamics of the simplified model is therefore similar to what we have already demonstrated for the model that includes a squeezed-vacuum bath. Such a similarity can be made closer by decreasing the ratio Ω/Δ, but at the expense of the DCE radiation strength. In the limit of $\Omega \ll \Delta$, the background noise is ≈ 0, so that all the photons radiated from the cavity can be thought of as the DCE photons. For realistic parameters $g_0 = 10\gamma_m$, $F = 15\gamma_m$, and $\Omega/\Delta = 0.1$, we could obtain $\langle a^\dagger a\rangle_{\rm ss} \approx 1.8 \times 10^{-3}$ at resonance ($\omega_m = \omega_d = 2\omega_s$). This results in an output flux $\approx 2.0 \times 10^4$ photons per second for $\kappa/2\pi = 2$ MHz. This radiation can be measured using single-photon detectors.

V. POSSIBLE IMPLEMENTATIONS

As an example, we consider an *LC* superconducting circuit with a micromechanical membrane (see Appendix D for details). In this device, the *LC* circuit is used to form a single-mode microwave cavity. The mechanical motion of the membrane modulates the capacitance of the *LC* circuit, and thus the cavity frequency. In order to squeeze the cavity mode, an additional tunable capacitor is embedded into the device. Its cosine-wave modulation serves as a two-photon driving for the cavity mode. The squeezed-vacuum reservoir can be generated through an *LC* circuit with a tunable capacitor, or through a Josephson parametric amplifier [50,58].

Alternatively, our proposal can be implemented in an optical system such as a whispering-gallery-mode (WGM) microresonator coupled to a mechanical breathing mode [59–65]. The WGM microresonator made from nonlinear crystals exhibits strong optical nonlinearities [66–68], which is the essential requirement for squeezing. The squeezed-vacuum reservoir for the optical cavity can be prepared by pumping a nonlinear medium, e.g., periodically poled $KTiOPO_4$ (PPKTP) crystal, in a cavity [69–72].

VI. CONCLUSIONS

We have introduced a method for how to observe the mechanical DCE in an optomechanical system. The method eliminates the problematic need for an extremely high mechanical-oscillation frequency and an ultrastrong single-photon optomechanical coupling. Thus, it paves an experimentally feasible path to observing quantum radiation from a moving mirror. Our method can be interpreted in the laboratory frame as mechanically induced two-photon hyper-Raman scattering, an anti-Stokes process of scattering a driving photon pair into a higher energy mode by absorbing a phonon. For the absorbed phonon, its annihilation indicates the creation of a real photon pair out of the quantum vacuum in the squeezed frame. We have also showed a surprising result: that the squeezing, which additionally induces and amplifies the DCE, can be extremely weak. Note that in this case, the unconventional DCE can be considered somehow similar to an unconventional photon blockade (UPB) [73]. Indeed, an UPB is induced by a nonlinearity, which can be extremely small. Finally, we expect that the approach presented here could find diverse applications in theoretical and experimental studies of quantum vacuum radiation.

ACKNOWLEDGMENTS

S.S. acknowledges the Army Research Office (ARO) (Grant No. W911NF1910065). F.N. was supported in part by the MURI Center for Dynamic Magneto-Optics via the Air Force Office of Scientific Research (AFOSR) (Grant No. FA9550-14-1-0040), Army Research Office (ARO) (Grant No. W911NF-18-1-0358), Asian Office of Aerospace Research and Development (AOARD) (Grant No. FA2386-18-1-4045), Japan Science and Technology Agency (JST) (via the Q-LEAP program, and CREST Grant No. JPMJCR1676), Japan Society for the Promotion of Science (JSPS) (JSPS-RFBR Grant No. 17-52-50023, and JSPS-FWO Grant No. VS.059.18N), the RIKEN-AIST Challenge Research Fund, the Foundational Questions Institute (FQXi), and the NTT PHI Labs.

APPENDIX A: OPTOMECHANICAL MASTER EQUATION, EFFECTIVE HAMILTONIAN, AND OFF-RESONANT SIGNAL-TO-NOISE RATIO

1. Optomechanical master equation

In order to evaluate the steady-state behavior of the system, its interaction with the environment needs to be described carefully. In our proposal for observing the DCE, we parametrically squeeze the cavity mode. Related methods have been used to enhance the light-matter interaction in optomechanical systems [44,45] and in cavity electrodynamics systems [46,47]. This can make the squeezed-cavity-mode (SCM) frequency comparable to the mechanical frequency, so that the mechanically induced DCE can be observed in a common optomechanical setup without the need for an ultrahigh mechanical frequency and an ultrastrong single-photon optomechanical coupling. However, the squeezing can also introduce undesired noise, including thermal noise and two-photon correlation, into the cavity. We can remove them by coupling a squeezed-vacuum bath to the bare-cavity mode. In this section, we give a detailed derivation of the master equation when the bare-cavity mode is coupled to a squeezed-vacuum bath and the mechanical mode is coupled to a thermal bath. We show that the noise induced by squeezing the cavity can be completely eliminated.

To begin with, we consider the Hamiltonian for the interaction between the system and the baths, which is given by

$$H_{\rm bath} = H^0_{\rm bath} + H^c_{\rm bath} + H^m_{\rm bath}, \tag{A1}$$

where

$$H_{\rm bath}^{0}=\sum_{l}\nu_{l}[t_{c}^{\dagger}(\nu_{l})t_{c}(\nu_{l})+t_{m}^{\dagger}(\nu_{l})t_{m}(\nu_{l})], \tag{A2}$$

$$H_{\rm bath}^{c}=\sum_{l}\lambda_{c}(\nu_{l})[a^{\dagger}t_{c}(\nu_{l})+t_{c}^{\dagger}(\nu_{l})a], \tag{A3}$$

$$H_{\rm bath}^{m}=\sum_{l}\lambda_{m}(\nu_{l})[b^{\dagger}t_{m}(\nu_{l})+t_{m}^{\dagger}(\nu_{l})b]. \tag{A4}$$

Here, $H_{\rm bath}^{0}$ is the free Hamiltonian of the baths, with $t_{c/m}(\nu_{l})$ the annihilation operators for the cavity and mechanical bath modes of frequency ν_{l}, and $H_{\rm bath}^{c/m}$ represent the couplings of the cavity and the mechanical resonator to their baths, with the coupling strengths $\lambda_{c/m}(\nu_{l})$ depending on the frequency ν_{l}. To derive the master equation, we first switch into the frame rotating at

$$H_{0}=\omega_{L}a^{\dagger}a/2+H_{\rm bath}^{0}, \tag{A5}$$

to introduce the SCM using the Bogoliubov transformation $a_{s}=\cosh(r)a+\sinh(r)a^{\dagger}$. Then, we again switch into the frame rotating at $H_{\rm CD}=\omega_{s}a_{s}^{\dagger}a_{s}$, with $\omega_{s}=\sqrt{\Delta^{2}-\Omega^{2}}$ being the SCM frequency, where $\Delta=\omega_{c}-\omega_{L}/2$ is the detuning between the bare-cavity frequency ω_{c} and the half frequency $\omega_{L}/2$ of the two-photon driving, and Ω is the two-photon driving amplitude. The couplings between the system and the baths are, accordingly, transformed to

$$H_{\rm bath}^{c}(t)=a(t)T_{c}^{\dagger}(t)+a^{\dagger}(t)T_{c}(t), \tag{A6}$$

$$H_{\rm bath}^{m}(t)=b(t)T_{m}^{\dagger}(t)+b^{\dagger}(t)T_{m}(t). \tag{A7}$$

Here, we have defined

$$a(t)=\exp(-i\omega_{L}t/2)\exp(iH_{\rm CD}t)a\exp(-iH_{\rm CD}t), \tag{A8}$$

$$b(t)=\exp(-i\omega_{m}t)b, \tag{A9}$$

$$T_{c}(t)=\sum_{\nu_{l}}\lambda_{c}(\nu_{l})t_{c}(\nu_{l})\exp(-i\nu_{l}t), \tag{A10}$$

$$T_{m}(t)=\sum_{\nu_{l}}\lambda_{m}(\nu_{l})t_{m}(\nu_{l})\exp(-i\nu_{l}t). \tag{A11}$$

Following the standard procedure in Ref. [40] and, then, returning to the frame rotating at H_{0}, we can obtain the following master equation expressed, in terms of the a_{s} mode:

$$\begin{aligned}\frac{d}{dt}\rho(t)=&\,i[\rho(t),H]\\&-\frac{\kappa}{2}(N+1)\mathcal{L}(a_{s})\rho(t)-\frac{\kappa}{2}N\mathcal{L}(a_{s}^{\dagger})\rho(t)\\&+\frac{\kappa}{2}M\mathcal{L}'(a_{s})\rho(t)+\frac{\kappa}{2}M^{*}\mathcal{L}'(a_{s}^{\dagger})\rho(t)\\&-\frac{\gamma_{m}}{2}(n_{\rm th}+1)\mathcal{L}(b)\rho(t)-\frac{\gamma_{m}}{2}n_{\rm th}\mathcal{L}(b^{\dagger})\rho(t),\end{aligned} \tag{A12}$$

where the Lindblad superoperators are defined by

$$\mathcal{L}(o)\rho(t)=o^{\dagger}o\rho(t)-2o\rho(t)o^{\dagger}+\rho(t)o^{\dagger}o, \tag{A13}$$

$$\mathcal{L}'(o)\rho(t)=oo\rho(t)-2o\rho(t)o+\rho(t)oo, \tag{A14}$$

and N, M are given, respectively, by

$$\begin{aligned}N=&\cosh^{2}(r)\sinh^{2}(r_{e})+\sinh^{2}(r)\cosh^{2}(r_{e})\\&+\tfrac{1}{2}\sinh(2r)\sinh(2r_{e})\cos(\theta_{e}),\end{aligned} \tag{A15}$$

$$\begin{aligned}M=&[\sinh(r)\cosh(r_{e})+\exp(-i\theta_{e})\cosh(r)\sinh(r_{e})]\\&\times[\cosh(r)\cosh(r_{e})+\exp(i\theta_{e})\sinh(r)\sinh(r_{e})],\end{aligned} \tag{A16}$$

corresponding to the thermal noise and two-photon correlation, and where

$$\kappa=2\pi d_{c}(\omega_{L}/2)\lambda_{c}^{2}(\omega_{L}/2), \tag{A17}$$

$$\gamma_{m}=2\pi d_{m}(\omega_{m})\lambda_{m}^{2}(\omega_{m}), \tag{A18}$$

represent, respectively, the cavity and mechanical decay rates, with $d_{c}(\omega_{L}/2)$ being the density of states for the cavity bath at frequency $\omega_{L}/2$, and $d_{m}(\omega_{m})$ being the density of states for the mechanical bath at frequency ω_{m}. Moreover, $n_{\rm th}=[\exp(\omega_{m}/k_{B}T)-1]^{-1}$ is the equilibrium phonon occupation at temperature T.

Note that, to derive the master equation in Eq. (A12), we have assumed that the central frequency of the squeezed-vacuum bath is equal to half the two-photon driving frequency. In addition, we have made the following approximations:

$$d_{c}(\omega_{L}/2\pm\omega_{s})\approx d_{c}(\omega_{L}/2), \tag{A19}$$

$$\lambda_{c}(\omega_{L}/2\pm\omega_{s})\approx\lambda_{c}(\omega_{L}/2). \tag{A20}$$

This is because, in our case, the SCM frequency ω_{s} is tuned to be comparable to the mechanical frequency ω_{m} ($\sim$MHz). Thus, it is much smaller than the two-photon driving frequency ω_{L} (of the order of GHz for microwave light or even THz for optical light).

According to Eqs. (A15) and (A16), we can have $N=M=0$ for $r_{e}=r$ and $\theta_{e}=\pm n\pi$ ($n=1,3,5,\ldots$), and thus, we have

$$\begin{aligned}\frac{d}{dt}\rho(t)=&\,i[\rho(t),H]-\frac{\kappa}{2}\mathcal{L}(a_{s})\rho(t)\\&-\frac{\gamma_{m}}{2}(n_{\rm th}+1)\mathcal{L}(b)\rho(t)-\frac{\gamma_{m}}{2}n_{\rm th}\mathcal{L}(b^{\dagger})\rho(t).\end{aligned} \tag{A21}$$

We find from Eq. (A21) that the squeezing-induced noise is completely eliminated, so that the a_{s} mode is equivalently coupled to the thermal vacuum bath. As we demonstrate below, eliminating this noise can ensure that the background noise is zero for the SCM excitation spectrum in the squeezed frame, and as a result, the background noise of the output-photon flux spectrum in the original laboratory frame only originates from photons contained in the squeezed vacuum. This minimizes the background noise for the observation of the DCE, and thus enables the DCE to be observed more clearly in experiments.

When the conditions $r=r_{e}$ and $\theta_{e}=\pm n\pi$ ($n=1,3,5,\ldots$) are not perfectly satisfied, the squeezing-induced noise cannot be eliminated completely (i.e., $N\neq 0$ and $M\neq 0$). However, according to the master equation in Eq. (A12), such imperfections do not affect the occurrence

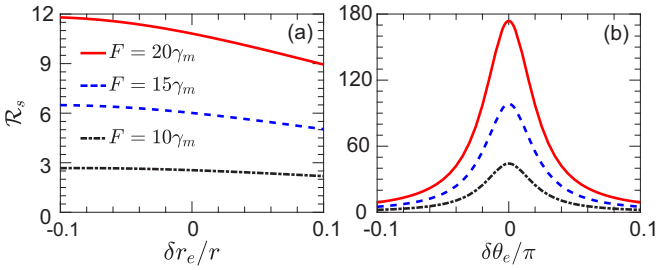

FIG. 4. Signal-to-noise ratio $\mathcal{R}_s$ versus (a) $\delta r_e = r_e - r$ and (b) $\delta\theta_e = \theta_e - \pi$ for the driving strength $F = 10\gamma_m$, $15\gamma_m$, and $20\gamma_m$. In (a), we set $\theta_e = 1.1\pi$, and in (b) $r_e = 1.1r$. In both plots, we set $g_0 = 10\gamma_m$, $n_{\rm th} = 0$, $\omega_m = \omega_d = 2\omega_s = 10^4\gamma_m$, $\Delta = \omega_m$, and $\kappa = 500\gamma_m$.

of the DCE. They only cause some noises. To quantify this undesired effect, we use the signal-to-noise ratio defined as

$$\mathcal{R}_s = \frac{\langle a_s^\dagger a_s\rangle_{\rm ss}^{F\neq 0} - \langle a_s^\dagger a_s\rangle_{\rm ss}^{F=0}}{\langle a_s^\dagger a_s\rangle_{\rm ss}^{F=0}}, \tag{A22}$$

where $\langle a_s^\dagger a_s\rangle_{\rm ss}^{F=0}$ ($\langle a_s^\dagger a_s\rangle_{\rm ss}^{F\neq 0}$) is the steady state $\langle a_s^\dagger a_s\rangle$ when $F = 0$ ($F \neq 0$), and the subscript "ss" stands for steady state. We plot $\mathcal{R}_s$ in Fig. 4, according to the master equation given in Eq. (A12) but replacing $H \mapsto H_{\rm eff}$. In this figure, we assume that $r_e = r + \delta r_e$ and $\theta_e = \pi + \delta\theta_e$. In the perfect case of $N = M = 0$, $\mathcal{R}_s \to \infty$ because $\langle a_s^\dagger a_s\rangle_{\rm ss}^{F=0} = 0$. Thus, we find in Fig. 4 that the noise induced by imperfect parameters reduces the ratio $\mathcal{R}_s$. However, we also find that with increasing the driving F, the noise becomes smaller compared to the DCE signal, such that it can even be neglected for sufficiently strong F.

2. Effective Hamiltonian

The Hamiltonian in Eqs. (A12) and (A21) is expressed, in terms of the a_s mode, as

$$\begin{aligned} H =& \omega_s a_s^\dagger a_s + \omega_m b^\dagger b - g_{\rm OM} a_s^\dagger a_s (b + b^\dagger) \\ &+ g_{\rm DCE}\left(a_s^2 + a_s^{\dagger 2}\right)(b + b^\dagger) \\ &+ \frac{F}{2}[\exp(i\omega_d t)b + \exp(-i\omega_d t)b^\dagger], \end{aligned} \tag{A23}$$

where $g_{\rm OM} = g_0\cosh(2r)$ and $g_{\rm DCE} = g_0\sinh(2r)/2$, with $r = (1/4)\ln[(\Delta + \Omega)/(\Delta - \Omega)]$ being the squeezing parameter of the cavity. In Fig. 5(a) we plot ω_s as a function of Δ and Ω, and find that the resonance condition $\omega_m = 2\omega_s$, for a parametric coupling between SCM and mechanical mode, can be achieved with experimentally modest parameters. The Hamiltonian H essentially describes the optomechanical system where the boundary condition of a squeezed field is modulated by the mechanical motion of a driven mirror. In the limit $\{\omega_s, \omega_m, \omega_d\} \gg \{g_{\rm OM}, g_{\rm DCE}, F\}$, we can apply the rotating-wave approximation, such that the coherent dynamics of the system is governed by the following effective Hamiltonian:

$$\begin{aligned} H_{\rm eff} =& \Delta_s a_s^\dagger a_s + \Delta_m b^\dagger b \\ &+ g_{\rm DCE}\left(a_s^2 b^\dagger + a_s^{\dagger 2} b\right) + \frac{F}{2}(b + b^\dagger), \end{aligned} \tag{A24}$$

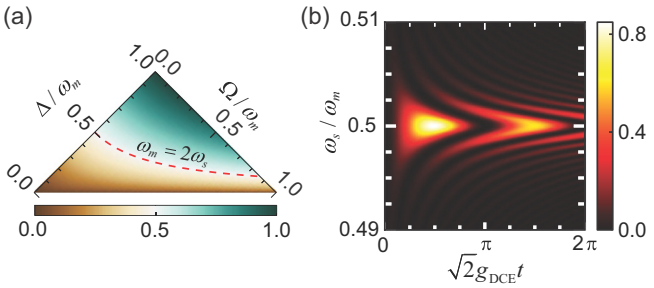

FIG. 5. (a) Squeezed-cavity-mode (SCM) frequency ω_s as a function of the parametric-driving detuning Δ and strength Ω. The dashed curve represents the $\omega_m = 2\omega_s$ case. Here, in order for the system to be stable, we need to have $\Delta > \Omega$. (b) Parametric energy conversion between the mechanical and squeezed cavity modes, obtained from a numerical solution of the master equation in Eq. (A21). Under the time evolution, a single phonon can simultaneously excite two SCM photons. Here, the initial state is $|0_{\rm s}, 1\rangle$ and the desired state is $|2_{\rm s}, 0\rangle$, where the first number in the ket refers to the SCM photon number and the second to the mechanical phonon number. Moreover, we set $g_0 = 80\gamma_m$, $n_{\rm th} = 0$, $\omega_m = 10^3 g_0$, $\Delta = \omega_m$, $\kappa = 10\gamma_m$, and $F = 0$.

where $\Delta_s = \omega_s - \omega_d/2$ and $\Delta_m = \omega_m - \omega_d$. The master equation in Eq. (A21) is then reduced to

$$\begin{aligned} \frac{d}{dt}\rho(t) =& i[\rho(t), H_{\rm eff}] - \frac{\kappa}{2}\mathcal{L}(a_s)\rho(t) \\ &- \frac{\gamma_m}{2}(n_{\rm th} + 1)\mathcal{L}(b)\rho(t) - \frac{\gamma_m}{2} n_{\rm th}\mathcal{L}(b^\dagger)\rho(t). \end{aligned} \tag{A25}$$

We find, according to Eq. (A24), that the coupling of the states $|0_{\rm s}, 1\rangle$ and $|2_{\rm s}, 0\rangle$, where the first number in the ket refers to the SCM photon number and the second one to the mechanical phonon number, is given by

$$g_{|0_{\rm s},1\rangle \leftrightarrow |2_{\rm s},0\rangle} = \sqrt{2} g_{\rm DCE}. \tag{A26}$$

In the squeezed frame, this means that under the time evolution, one phonon can be converted into two photons, and vice versa, at resonance $\omega_m = 2\omega_s$. To confirm such a state conversion, we perform numerics, as shown in Fig. 5(b). Specifically, we use the master equation in Eq. (A21) to calculate the fidelity, $\mathcal{F} = \langle 2_{\rm s}, 0|\rho_{\rm actual}(t)|2_{\rm s}, 0\rangle$, where $\rho_{\rm actual}(t)$ is the actual state. It is seen in Fig. 5(b) that we have the expected state conversion between light and mechanics, and there is a maximum conversion at resonance. Note that owing to the presence of the cavity and mechanical losses, the maximum conversion fidelity decreases with time.

To describe the dynamics of the DCE further, we plotted the time evolution of $\langle a_s^\dagger a_s\rangle$ in the presence of the driving F in Fig. 6. We find that $\langle a_s^\dagger a_s\rangle$ increases with time and then gradually approaches its stationary value. For an experimental parameter $\gamma_m \approx 200$ Hz in Ref. [74], the stationary state is reached within a time $\approx 5/\gamma_m \approx 25$ ms.

In Eq. (A24), we made the rotating-wave approximation and neglected the high-frequency component,

$$\begin{aligned} H_{\rm high} =& -g_{\rm OM} a_s^\dagger a_s[\exp(-i\omega_d t)b + \exp(i\omega_d t)b^\dagger] \\ &+ g_{\rm DCE}\left[\exp(-i2\omega_d t)a_s^2 b + \exp(i2\omega_d t)a_s^{\dagger 2} b^\dagger\right]. \end{aligned} \tag{A27}$$

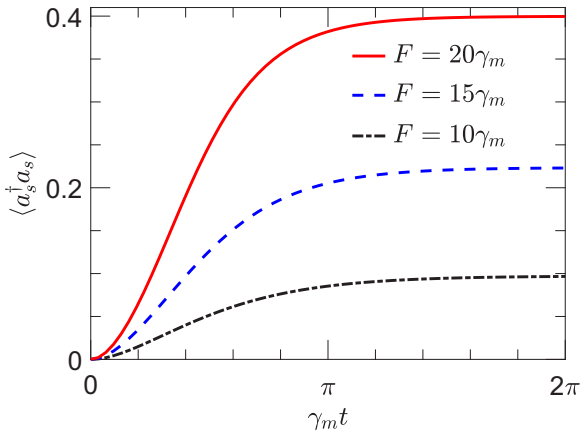

FIG. 6. Time evolution of $\langle a_s^\dagger a_s \rangle$ for the driving strength $F = 10\gamma_m$, $15\gamma_m$, and $20\gamma_m$, calculated from the master equation in Eq. (A25). Here, the initial state is assumed to be $|0_s, 0\rangle$. Furthermore, we assume that $g_0 = 10\gamma_m$, $n_{\rm th} = 0$, $\omega_m = \omega_d = 2\omega_s = 10^4\gamma_m$, $\Delta = \omega_m$, and $\kappa = 500\gamma_m$.

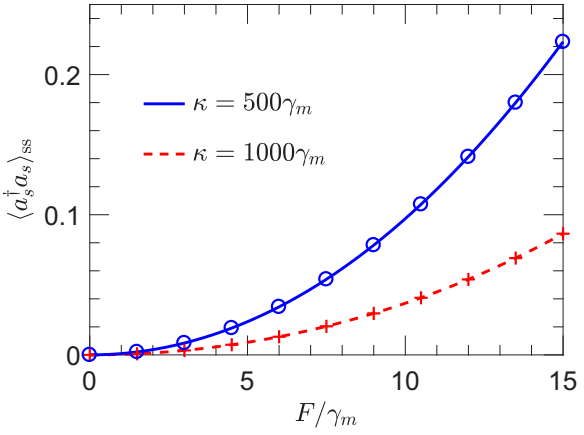

FIG. 7. Effects of the high-frequency component $H_{\rm high}$ on the photon number $\langle a_s^\dagger a_s \rangle_{\rm ss}$. The master equation used for curves is given in Eq. (A25), and for symbols is given in Eq. (A21) but with H in Eq. (A29). Here, we set $g_0 = 10\gamma_m$, $n_{\rm th} = 0$, $\omega_m = \omega_d = 2\omega_s = 10^4\gamma_m$, and $\Delta = \omega_m$.

In typical situations, $\{g_{\rm OM}, g_{\rm DCE}\} \ll \omega_d$, which allows a time-averaging treatment of $H_{\rm high}$ using the formalism of Ref. [75]. After a straightforward calculation, the behavior of $H_{\rm high}$ can be approximated, at resonance $\omega_m = \omega_d = 2\omega_s$ (i.e., $\Delta_s = \Delta_m = 0$), as

$$H_{\rm high} \approx H_{\rm TA} = -\frac{g_{\rm OM}^2}{\omega_m}(a_s^\dagger a_s)^2 - \frac{g_{\rm DCE}^2}{2\omega_m}\big[a_s^{\dagger 2}a_s^2 + 2(2a_s^\dagger a_s + 1)b^\dagger b + 2(2a_s^\dagger a_s + 1)\big]. \quad \text{(A28)}$$

The Hamiltonian H is, accordingly, transformed to

$$H \approx H_{\rm eff} + H_{\rm TA}. \quad \text{(A29)}$$

For realistic parameters, the couplings $g_{\rm OM}$ and $g_{\rm DCE}$ are three orders of magnitude lower than ω_m. We can find from Eq. (A28) that the high-frequency term $H_{\rm high}$ can be neglected, compared to the low-frequency term $H_{\rm eff}$. To confirm this, in Fig. 7 we numerically calculated $\langle a_s^\dagger a_s \rangle_{\rm ss}$ using the low-frequency term $H_{\rm eff}$ and the full Hamiltonian H given in Eq. (A29), respectively. By comparing these, we find an excellent agreement, and the high-frequency term $H_{\rm high}$ can be safely neglected, as expected.

3. Off-resonant signal-to-noise ratio

In the main text, the signal-to-noise ratio $\mathcal{R}$ is discussed at resonance $\omega_m = \omega_d = 2\omega_s$ (i.e., $\Delta_s = \Delta_m = 0$). We now discuss the ratio $\mathcal{R}$ in the off-resonance case where $\Delta_s \neq 0$ and $\Delta_m \neq 0$. We plot the ratio $\mathcal{R}$ as a function of the detunings Δ_s and Δ_m in Fig. 8. There, the results are obtained by numerically integrating the master equation in Eq. (A25). We find that the ratio $\mathcal{R}$ decreases with the detuning Δ_s or Δ_m, but increases with the force F. Note that the DCE photons are the scattered photon pairs via two-photon hyper-Raman scattering. As a result, their frequency $\omega_s + \omega_L/2$ is different from the noise-photon frequency $\omega_L/2$. This means that if standard techniques of Raman spectroscopy are used, the noise can then be filtered out. Therefore, the signal can still be resolved even if $R < 1$.

APPENDIX B: DYNAMICAL CASIMIR EFFECT IN THE MECHANICAL WEAK-DRIVING REGIME

In our main text, we have studied the steady-state behavior associated with the DCE, by numerically integrating the master equation in Eq. (A25) [76,77]. To study the DCE further, an analytical understanding for the mechanical weak driving is given in this Appendix. Here, we only focus on the resonance situation where $\omega_m = \omega_d = 2\omega_s$.

Let us now derive the steady-state SCM photon number $\langle a_s^\dagger a_s \rangle_{\rm ss}$. To begin, we consider the master equation in Eq. (A25). The involved equations of motion are given, respectively, by

$$\frac{d}{dt}\langle a_s^\dagger a_s \rangle = -4g_{\rm DCE}\,{\rm Im}\big[\langle a_s^2 b^\dagger \rangle\big] - \kappa\langle a_s^\dagger a_s \rangle, \quad \text{(B1)}$$

$$\frac{d}{dt}\langle a_s^2 \rangle = -i2g_{\rm DCE}(2\langle a_s^\dagger a_s b\rangle + \langle b\rangle) - \kappa\langle a_s^2\rangle, \quad \text{(B2)}$$

$$\frac{d}{dt}\langle b\rangle = -i\left(g_{\rm DCE}\langle a_s^2\rangle + \frac{F}{2}\right) - \frac{\gamma_m}{2}\langle b\rangle, \quad \text{(B3)}$$

$$\frac{d}{dt}\langle b^\dagger b\rangle = 2g_{\rm DCE}\,{\rm Im}\big[\langle a_s^2 b^\dagger\rangle\big] - F\,{\rm Im}[\langle b\rangle] - \gamma_m\langle b^\dagger b\rangle + \gamma_m n_{\rm th}, \quad \text{(B4)}$$

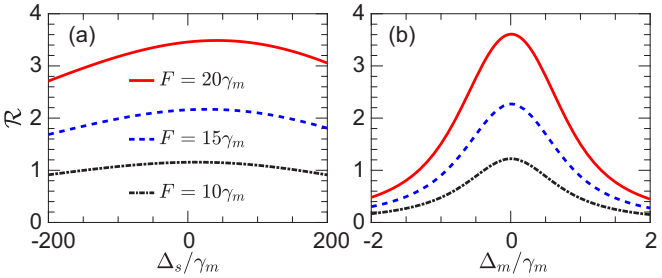

FIG. 8. Signal-to-noise ratio $\mathcal{R}$ versus detunings (a) Δ_s and (b) Δ_m for the driving strength $F = 10\gamma_m$, $15\gamma_m$, and $20\gamma_m$. The master equation used here is given in Eq. (A25). In (a), we set $\Delta_m = 0.2\gamma_m$ and in (b) $\Delta_s = 10\gamma_m$. In both plots, we set $g_0 = 10\gamma_m$, $n_{\rm th} = 0$, $\kappa = 500\gamma_m$, and $\sinh^2(r) = 0.5$.

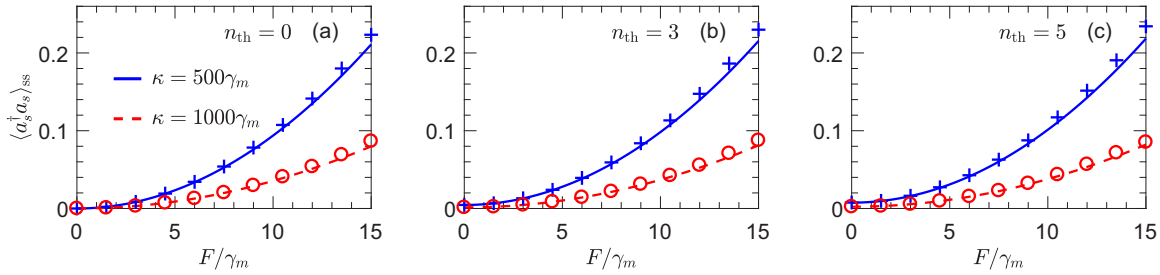

FIG. 9. Photon number $\langle a_s^\dagger a_s\rangle_{\rm ss}$ versus mechanical driving F for (a) $n_{\rm th}=0$, (b) $n_{\rm th}=3$, and (c) $n_{\rm th}=5$. Curves are analytical results, while symbols are numerical simulations of the master equation in Eq. (A25). Here, we set $g_0=10\gamma_m$, $\omega_m=\omega_d=2\omega_s=10^4\gamma_m$, and $\Delta=\omega_m$.

$$\frac{d}{dt}\langle a_s^2 b^\dagger\rangle = i\Big(g_{\rm DCE}\langle a_s^{\dagger 2}a_s^2\rangle - 4g_{\rm DCE}\langle a_s^\dagger a_s b^\dagger b\rangle + \frac{F}{2}\langle a_s^2\rangle - 2g_{\rm DCE}\langle b^\dagger b\rangle\Big) - \Big(\kappa+\frac{\gamma_m}{2}\Big)\langle a_s^2 b^\dagger\rangle, \tag{B5}$$

$$\frac{d}{dt}\langle a_s^\dagger a_s b\rangle = ig_{\rm DCE}\big(2\langle a_s^2 b^\dagger b\rangle - \langle a_s^\dagger a_s^3\rangle - 2\langle a_s^{\dagger 2}b^2\rangle\big) - i\frac{F}{2}\langle a_s^\dagger a_s\rangle - \Big(\kappa+\frac{\gamma_m}{2}\Big)\langle a_s^\dagger a_s b\rangle. \tag{B6}$$

Here, Im[z] represents the imaginary part of z. In fact, owing to the parametric coupling, the Hamiltonian in Eq. (A24) leads to an infinite set of differential equations, which may not be analytically solved. Thus, in order to obtain an analytical result, we neglect the higher-order correlation terms, that is $\langle a_s^{\dagger 2}a_s^2\rangle$, $\langle a_s^\dagger a_s b^\dagger b\rangle$, $\langle a_s^2 b^\dagger b\rangle$, $\langle a_s^\dagger a_s^3\rangle$, and $\langle a_s^{\dagger 2}b^2\rangle$. This approximation is valid for a weak driving F, as shown below. In such an approximation, the coupled differential equations (B1)–(B6) construct a closed set, so in the steady state we have

$$0 \approx -4g_{\rm DCE}\ {\rm Im}\big[\langle a_s^2 b^\dagger\rangle_{\rm ss}\big] - \kappa\langle a_s^\dagger a_s\rangle_{\rm ss}, \tag{B7}$$

$$0 \approx -i2g_{\rm DCE}(2\langle a_s^\dagger a_s\rangle_{\rm ss} + \langle b\rangle_{\rm ss}) - \kappa\langle a_s^2\rangle_{\rm ss}, \tag{B8}$$

$$0 \approx -i\Big(g_{\rm DCE}\langle a_s^2\rangle_{\rm ss} + \frac{F}{2}\Big) - \frac{\gamma_m}{2}\langle b\rangle_{\rm ss}, \tag{B9}$$

$$0 \approx 2g_{\rm DCE}\ {\rm Im}\big[\langle a_s^2 b^\dagger\rangle_{\rm ss}\big] - F\ {\rm Im}[\langle b\rangle_{\rm ss}] - \gamma_m\langle b^\dagger b\rangle_{\rm ss} + \gamma_m n(\omega_m, T), \tag{B10}$$

$$0 \approx i\Big(\frac{F}{2}\langle a_s^2\rangle - 2g_{\rm DCE}\langle b^\dagger b\rangle_{\rm ss}\Big) - \Big(\kappa+\frac{\gamma_m}{2}\Big)\langle a_s^2 b^\dagger\rangle_{\rm ss}, \tag{B11}$$

$$0 \approx -i\frac{F}{2}\langle a_s^\dagger a_s\rangle_{\rm ss} - \Big(\kappa+\frac{\gamma_m}{2}\Big)\langle a_s^\dagger a_s b\rangle_{\rm ss}. \tag{B12}$$

By solving this closed set of equations, the steady-state SCM photon number is found to be

$$\langle a_s^\dagger a_s\rangle_{\rm ss} \approx \frac{4\gamma_m g_{\rm DCE}^2}{\kappa\big(2g_{\rm DCE}^2+\gamma_0^2\big)}\left[\frac{\kappa F^2}{2\gamma_m\big(2g_{\rm DCE}+\gamma_0^2\big)} + n_{\rm th}\right], \tag{B13}$$

where $\gamma_0=\sqrt{\kappa\gamma_m/2}$. Equation (B13) shows that $\langle a_s^\dagger a_s\rangle_{\rm ss}$ includes two physical contributions: one from the mechanical driving and the other from the thermal noise. Furthermore, we also find a quadratic increase in $\langle a_s^\dagger a_s\rangle_{\rm ss}$ with the driving F. To confirm this analytical expression, in Fig. 9 we compare it with exact numerical simulations of the master equation in Eq. (A25). It is seen that the analytical predictions are in good agreement with the exact numerical results, especially for weak F.

According to the Bogoliubov transformation, the steady-state intracavity-photon number $\langle a^\dagger a\rangle_{\rm ss}$ in the original laboratory frame is given in Eq. (12). Then, the steady-state output-photon flux is given in Eq. (14). To obtain $\Phi_{\rm out}$ analytically, the physical quantities $\langle a_s^\dagger a_s\rangle_{\rm ss}$ and Re$[\langle a_s^2\rangle_{\rm ss}]$ are involved, as shown in Eq. (13). The steady-state SCM photon number, $\langle a_s^\dagger a_s\rangle_{\rm ss}$, is given in Eq. (B13), and further is numerically confirmed in Fig. 9. From the closed set of the steady-state equations given in Eqs. (B7)–(B12), we can straightforwardly find

$$\langle a_s^2\rangle_{\rm ss} = -\frac{g_{\rm DCE}}{2g_{\rm DCE}^2+\gamma_0^2}F. \tag{B14}$$

It shows that $|{\rm Re}[\langle a_s^2\rangle_{\rm ss}]|$ increases linearly with F but is independent of the thermal mechanical noise. This behavior is also numerically confirmed in Fig. 10, showing a good agreement especially for the weak driving F. Note that the derivation of the analytical results and their numerical confirmations originates from neglecting the higher-order correlation terms. In order to exactly describe $\langle a_s^2\rangle$, such higher-order correlations should be included. By combining Eqs. (B13) and (B14), the steady-state output-photon flux can be analytically expressed as

$$\Phi_{\rm out} = 4\frac{4\gamma_m g_{\rm DCE}^2}{\kappa\big(2g_{\rm DCE}^2+\gamma_0^2\big)}\left[\frac{\kappa}{2\gamma_m\big(2g_{\rm DCE}+\gamma_0^2\big)}F^2 + n_{\rm th}\right] \times \cosh(2r) + \frac{g_{\rm DCE}}{2g_{\rm DCE}^2+\gamma_0^2}\sinh(2r)F + \kappa\sinh^2(r). \tag{B15}$$

We find from Eq. (B15) that, by increasing the mechanical driving F, the DCE-induced photon flux $\Phi_{\rm DCE}$ becomes stronger quadratically, but at the same time, the background-noise photon flux $\Phi_{\rm BGN}$ remains unchanged. Therefore, the increase in the total photon flux $\Phi_{\rm out}$ with F can be considered as a signature of the mechanical-motion induced DCE.

In the DCE process, the photons are emitted in pairs, and therefore, they could exhibit photon bunching [25,36,57]. The essential parameter quantifying this property is the equal-time second-order correlation function, defined in Eq. (17). We now derive this second-order correlation function. The

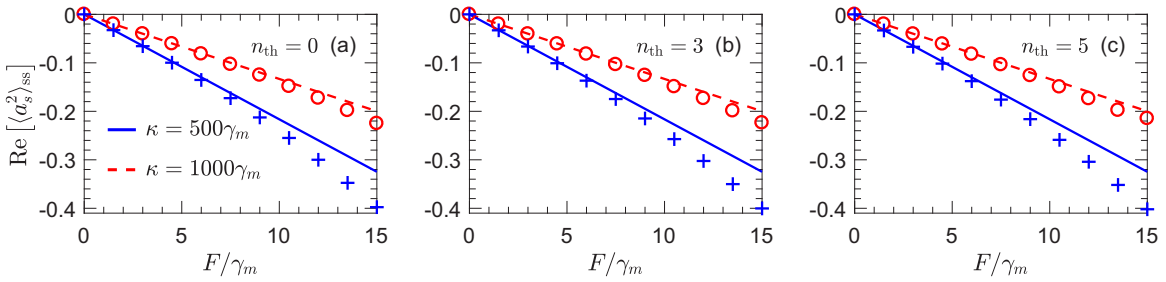

FIG. 10. Real part of the correlation function $\langle a_s^2\rangle_{\rm ss}$ versus mechanical driving F for (a) $n_{\rm th}=0$, (b) $n_{\rm th}=3$, and (c) $n_{\rm th}=5$. We assumed the same curve correspondences and the same parameters as in Fig. 9.

equation of motion for $\langle a_s^{\dagger 2}a_s^2\rangle$ is given by

$$\frac{d}{dt}\langle a_s^{\dagger 2}a_s^2\rangle = -4g_{\rm DCE}\{2{\rm Im}[\langle a_s^\dagger a_s^3 b^\dagger\rangle]+{\rm Im}[\langle a_s^2 b^\dagger\rangle]\} - 2\kappa\langle a_s^{\dagger 2}a_s^2\rangle. \tag{B16}$$

We can neglect the term ${\rm Im}[\langle a_s^\dagger a_s^3 b^\dagger\rangle]$ for the weak driving F. Then, combining Eq. (B7) yields

$$g_s^{(2)}(0)\approx\frac{1}{2\langle a_s^\dagger a_s\rangle_{\rm ss}}. \tag{B17}$$

In Fig. 11, we plot the $g_s^{(2)}(0)$ correlation as a function of the driving F. In this figure, we compare the analytical and numerical results, and show an exact agreement. Owing to a very small of $\langle a_s^\dagger a_s\rangle_{\rm ss}$ for the mechanical weak driving, $g_s^{(2)}(0)$ is very large as shown in Fig. 11, which corresponds to large photon bunching. With increasing the driving F, we also find that the $g_s^{(2)}(0)$ correlation decreases, and as demonstrated more explicitly in Appendix C, it would approach a lower bound equal to 1, thereby implying that the DCE radiation field becomes a coherent state in the limit of the mechanical strong driving, $F\to\infty$.

APPENDIX C: SEMICLASSICAL TREATMENT FOR THE DYNAMICAL CASIMIR EFFECT

In Appendix B we have analytically discussed the DCE process when the mechanical driving F is weak. There, the higher-order correlations that arise from the parametric coupling are neglected, and the resulting expressions can predict the system behavior well. For strong-F driving, all high-order correlations should be included to exactly describe the system; but in this case, finding solutions analytically or even numerically becomes much more difficult. In order to investigate the DCE in the strong-F regime, in this section we employ a semiclassical treatment [56]. For simplicity, but without loss of generality, here we assume that the mechanical resonator is coupled to a zero-temperature bath. For finite temperatures, the discussion below is still valid, as long as the total number of phonons is much larger than the number of thermal phonons.

1. Excitation spectrum and output-photon flux spectrum in the steady state

We again begin with the master equation in Eq. (A25) and, accordingly, obtain

$$\frac{d}{dt}\langle a_s^\dagger a_s\rangle = -4g_{\rm DCE}\,{\rm Im}\left[\langle a_s^2\rangle\langle b\rangle^*\right]-\kappa\langle a_s^\dagger a_s\rangle, \tag{C1}$$

$$\frac{d}{dt}\langle a_s^2\rangle = -i2\Delta_s\langle a_s^2\rangle - i2g_{\rm DCE}(2\langle a_s^\dagger a_s\rangle+1)\langle b\rangle-\kappa\langle a_s^2\rangle, \tag{C2}$$

$$\frac{d}{dt}\langle b\rangle = -i\left(\Delta_m\langle b\rangle+g_{\rm DCE}\langle a_s^2\rangle+\frac{F}{2}\right)-\frac{\gamma_m}{2}\langle b\rangle. \tag{C3}$$

Here, we have made the semiclassical approximation, such that $\langle a_s^2 b^\dagger\rangle\approx\langle a_s^2\rangle\langle b\rangle^*$ and $\langle a_s^\dagger a_s b\rangle\approx\langle a_s^\dagger a_s\rangle\langle b\rangle$. Under this approximation, the fluctuation correlation between the cavity and the mechanical resonator is neglected. It is found that Eqs. (C1)–(C3) construct a closed set.

a. Excitation spectrum for resonant mechanical driving: $\omega_m=\omega_d$

We first consider the case of a resonant mechanical driving (i.e., $\omega_m=\omega_d$). In this case, we have $\Delta_m=0$, and the steady-state SCM photon number $\langle a_s^\dagger a_s\rangle_{\rm ss}$ satisfies a cubic

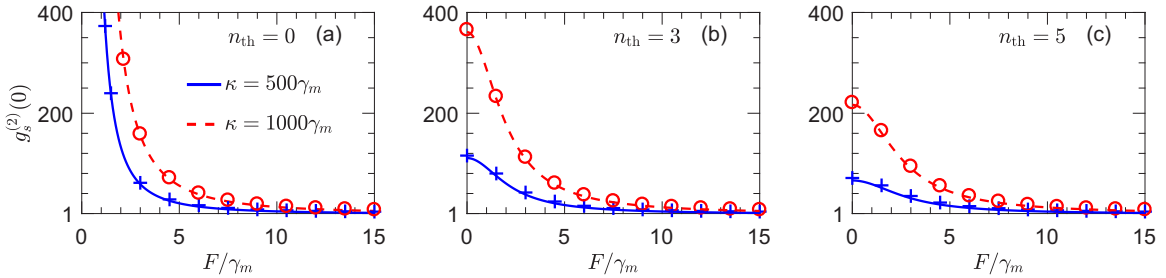

FIG. 11. Correlation function $g_s^{(2)}(0)$ versus mechanical driving F for (a) $n_{\rm th}=0$, (b) $n_{\rm th}=3$, and (c) $n_{\rm th}=5$. We assumed the same curve correspondences and the same parameters as in Fig. 9.

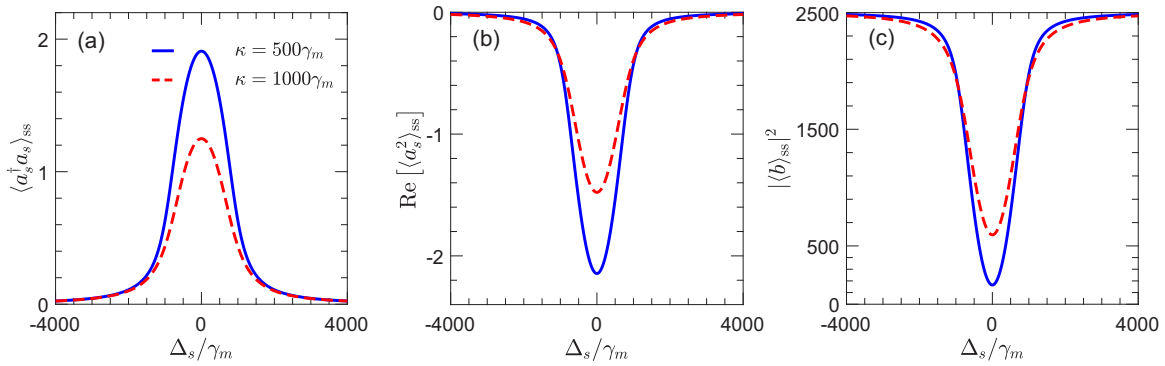

FIG. 12. (a) Photon number $\langle a_s^\dagger a_s\rangle_{ss}$, (b) real part of the correlation function $\langle a_s^2\rangle_{ss}$, and (c) phonon number $|\langle b\rangle_{ss}|^2$ versus detuning $\Delta_s = \omega_s - \omega_d/2$ for $\kappa = 500\gamma_m$ (solid curves) and $\kappa = 1000\gamma_m$ (dashed curves). We have assumed that $\omega_m = \omega_d$, $g_0 = 10\gamma_m$, $F = 50\gamma_m$, and $\sinh^2(r) = 0.5$.

equation,

$$0 = g_{\mathrm{DCE}}^4 x^3 - g_{\mathrm{DCE}}^2\left(g_{\mathrm{DCE}}^2 - \gamma_0^2\right)x^2 + \left[\tfrac{1}{4}\left(\Delta_s^2\gamma_m^2 + \gamma_0^4\right) - g_{\mathrm{DCE}}^2\left(F^2 + \gamma_0^2\right)\right]x - \tfrac{1}{4}\left(\Delta_s^2\gamma_m^2 + \gamma_0^4\right), \tag{C4}$$

where $\gamma_0 = \sqrt{\kappa\gamma_m/2}$ and $x = 2\langle a_s^\dagger a_s\rangle_{ss} + 1$. The solutions of such an equation can be exactly obtained using the Cardano formula. Then, the steady-state $\langle a_s^2\rangle$ and $\langle b\rangle$ are given, respectively, by

$$\left\langle a_s^2\right\rangle_{ss} = -\frac{g_{\mathrm{DCE}}}{2g_{\mathrm{DCE}}^2 x + \gamma_0^2 + i\Delta_s\gamma_m}Fx, \tag{C5}$$

$$\langle b\rangle_{ss} = -\frac{(-2\Delta_s + i\kappa)}{2g_{\mathrm{DCE}}^2 x + \gamma_0^2 + i\Delta_s\gamma_m}\frac{F}{2}. \tag{C6}$$

For simplicity, we numerically solve the cubic equation (C4), and in Fig. 12 we plot $\langle a_s^\dagger a_s\rangle_{ss}$, $\mathrm{Re}[\langle a_s^2\rangle_{ss}]$, and $|\langle b\rangle_{ss}|^2$ versus the detuning Δ_s for $\kappa = 500\gamma_m$ and $1000\gamma_m$. At large detunings, the resonantly driven mechanical resonator is effectively decoupled from the cavity mode. As a consequence, there is almost no conversion of mechanical energy into photons. Thus at large detunings, the mechanical phonon number $|\langle b\rangle_{ss}|^2$ quickly approaches $(F/\gamma_m)^2$, i.e., the steady-state phonon number when the mechanical resonator is completely uncoupled. Meanwhile, both the photon number $\langle a_s^\dagger a_s\rangle_{ss}$ and correlation function $\langle a_s^2\rangle_{ss}$ are very close to zero. As the detuning decreases, the effective parametric coupling between the mechanical motion and the cavity mode increases, and the parametric conversion from mechanical energy into photons is accordingly enhanced. Such an energy conversion is maximized at resonance $\omega_m = \omega_d = 2\omega_s$. Thus, when decreasing the detuning, both $\langle a_s^\dagger a_s\rangle_{ss}$ and $|\mathrm{Re}[\langle a_s^2\rangle_{ss}]|$ increase but $|\langle b\rangle_{ss}|^2$ decreases, as shown in Fig. 12. In particular, $\langle a_s^\dagger a_s\rangle_{ss}$ and $|\mathrm{Re}[\langle a_s^2\rangle_{ss}]|$ reach their maximum values at resonance, and at the same time, $|\langle b\rangle_{ss}|^2$ reaches its minimum value. This behavior implies that the photons are emitted by the mechanical resonator.

b. Excitation spectrum for resonant parametric coupling: $\omega_m = 2\omega_s$

We next consider the case of a resonant parametric coupling (i.e., $\omega_m = 2\omega_s$). In this case, we have $\Delta_m = 2\Delta_s = \Delta$, and the steady-state $\langle a_s^\dagger a_s\rangle$ also satisfies a cubic equation

$$0 = g_{\mathrm{DCE}}^4 x^3 - g_{\mathrm{DCE}}^2\left(g_{\mathrm{DCE}}^2 + \Delta^2 - \gamma_0^2\right)x^2 + \left\{\tfrac{1}{4}\left[\left(\Delta^2 - \gamma_0^2\right)^2 + \Delta^2\gamma_1^2\right] + g_{\mathrm{DCE}}^2 \times \left(\Delta^2 - \gamma_0^2 - F^2\right)\right\}x - \tfrac{1}{4}\left[\left(\Delta^2 - \gamma_0^2\right)^2 + \Delta^2\gamma_1^2\right], \tag{C7}$$

where $\gamma_1 = \kappa + \gamma_m/2$. This cubic equation can also be exactly solved using the Cardano formula, and then the steady-state $\langle a_s^2\rangle$ and $\langle b\rangle$ are given, respectively, by

$$\left\langle a_s^2\right\rangle_{ss} = -\frac{g_{\mathrm{DCE}}}{2g_{\mathrm{DCE}}x - \Delta^2 + \gamma_0^2 + i\Delta\gamma_1}Fx, \tag{C8}$$

$$\langle b\rangle_{ss} = -\frac{(-\Delta + i\kappa)}{2g_{\mathrm{DCE}}x - \Delta^2 + \gamma_0^2 + i\Delta\gamma_1}\frac{F}{2}. \tag{C9}$$

We numerically solve the cubic equation (C7), and in Fig. 13, we plot $\langle a_s^\dagger a_s\rangle_{ss}$, $\mathrm{Re}[\langle a_s^2\rangle_{ss}]$, and $|\langle b\rangle_{ss}|^2$ versus the detuning Δ_s for $\kappa = 500\gamma_m$ and $1000\gamma_m$. At large detunings, the mechanical driving is effectively decoupled from the mechanical resonator, so that almost no phonons are excited and almost no photons are emitted. As the detuning decreases, the mechanical phonon number increases, which strengthens the parametric conversion from mechanical energy into photons, and in turn, leads to an increase in the excited photon number. This process is maximized at resonance $\omega_m = \omega_d = 2\omega_s$. Thus, we find that, as shown in Fig. 13, with decreasing the detuning, not only $\langle a_s^\dagger a_s\rangle_{ss}$ and $|\mathrm{Re}[\langle a_s^2\rangle_{ss}]|$ but also $|\langle b\rangle_{ss}|^2$ increases, and that they simultaneously reach their maximum values at resonance. This behavior also implies that the photons are emitted by the mechanical resonator.

c. Output-photon flux spectrum for resonant mechanical driving and parametric coupling

Having obtained $\langle a_s^\dagger a_s\rangle_{ss}$ and $\langle a_s^2\rangle_{ss}$ in the squeezed frame, we can, according to the Bogoliubov transformation, calculate the steady-state intracavity photon number $\langle a^\dagger a\rangle_{ss}$ in the

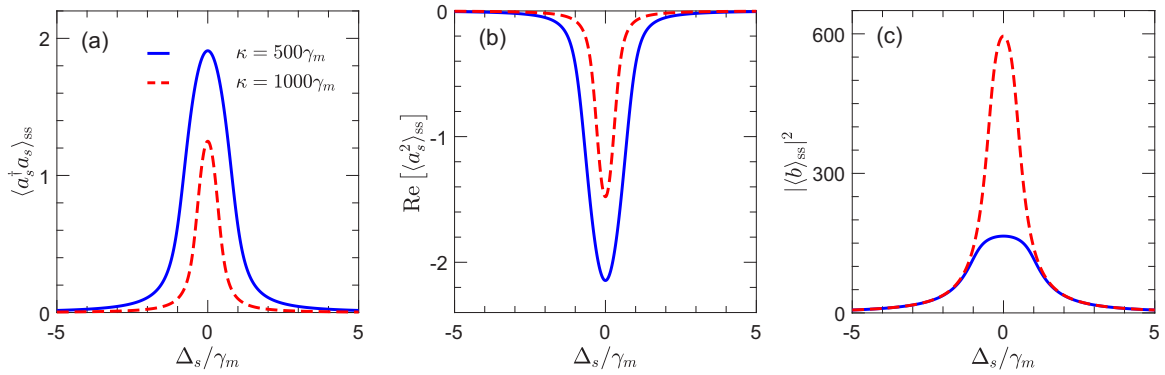

FIG. 13. (a) Photon number $\langle a_s^\dagger a_s\rangle_{ss}$, (b) real part of the correlation function $\langle a_s^2\rangle_{ss}$, and (c) phonon number $|\langle b\rangle_{ss}|^2$ (c) versus detuning $\Delta_s = \omega_s - \omega_d/2$ for $\kappa = 500\gamma_m$ (solid curves) and $\kappa = 1000\gamma_m$ (dashed curves). We have assumed that $\omega_m = 2\omega_s$, $g_0 = 10\gamma_m$, $F = 50\gamma_m$, and $\sinh^2(r) = 0.5$.

original laboratory frame, as given in Eq. (12). Then we can calculate the steady-state output-photon flux $\Phi_{\rm out}$ according to the input-output relation, given in Eq. (14). We plot the photon flux $\Phi_{\rm out}$ as a function of the detuning Δ_s in Fig. 14. As expected, for a given mechanical driving, we can observe a resonance peak, corresponding to the maximum value of the photon flux. This behavior in the laboratory frame can directly reflect the behavior of the excitation spectrum $\langle a_s^\dagger a_s\rangle_{ss}(\Delta_s)$ in the squeezed frame in Figs. 12(a) and 13(a). This is because the background noise $\Phi_{\rm BGN}$ remains unchanged when the detuning is changed, and the peak completely arises from the DCE in the squeezed frame. Thus, the appearance of the peak of the output flux spectrum $\Phi_{\rm out}(\Delta_s)$ can be considered as an experimentally observable signature of the DCE.

2. Signal-to-noise ratio and second-order correlation function at resonance

As mentioned before, there exists a background noise $\Phi_{\rm BGN}$ in the flux $\Phi_{\rm out}$. Thus, we need to analyze the ability of our proposal to resolve the DCE-induced signal from the background noise. To quantitatively describe this ability, we typically employ the signal-to-noise ratio defined in Eq. (15). Without loss of generality, we focus on the ratio $\mathcal{R}$ at resonance $\omega_m = \omega_d = 2\omega_s$. Under this resonance condition, the cubic equation satisfied by $\langle a_s^\dagger a_s\rangle_{ss}$ becomes

$$0 = g_{\rm DCE}^4 x^3 - g_{\rm DCE}^2\left(g_{\rm DCE}^2 - \gamma_0^2\right)x^2 + \left[\frac{\gamma_0^4}{4} - g_{\rm DCE}^2\left(\gamma_0^2 + F^2\right)\right]x - \frac{\gamma_0^4}{4}, \tag{C10}$$

where $x = 2\langle a_s^\dagger a_s\rangle + 1$. Then, $\langle a_s^2\rangle_{ss}$ and $\langle b\rangle_{ss}$ are given by

$$\langle a_s^2\rangle_{ss} = -\frac{g_{\rm DCE}}{2g_{\rm DCE}^2 x + \gamma_0^2}Fx, \tag{C11}$$

$$\langle b\rangle_{ss} = -\frac{i\kappa}{2g_{\rm DCE}^2 x + \gamma_0^2}\frac{F}{2}. \tag{C12}$$

We plot the ratio $\mathcal{R}$ versus the driving F in Fig. 15(a). We find that the signal-to-noise ratio monotonically increases with the mechanical driving. This is owing to the fact that an increase in the mechanical driving leads to an increase in the number of DCE-induced photons, but at the same time leaves the number of background-noise photons unchanged.

The equal-time second-order correlation function is defined in Eq. (17). Similarly to the discussion of the signal-to-noise ratio $\mathcal{R}$, we also only focus on the $g_s^{(2)}(0)$ correlation at resonance $\omega_m = \omega_d = 2\omega_s$. In the semiclassical treatment presented in this section, $\langle a_s^{\dagger 2} a_s^2\rangle_{ss}$ can be approximated as $\langle a_s^{\dagger 2} a_s^2\rangle_{ss} \approx |\langle a_s^2\rangle_{ss}|^2$, and as a result, the $g_s^{(2)}(0)$ correlation is reduced to

$$g_s^{(2)}(0) \approx \frac{\left|\langle a_s^2\rangle_{ss}\right|^2}{\langle a_s^\dagger a_s\rangle_{ss}^2}, \tag{C13}$$

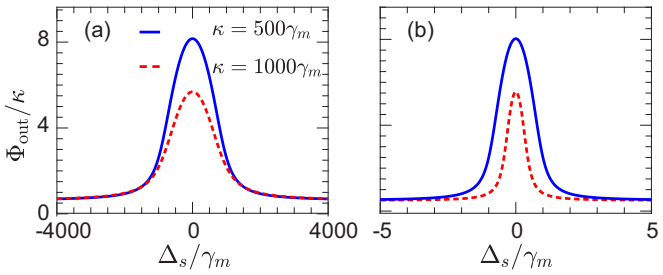

FIG. 14. Steady-state output-photon flux $\Phi_{\rm out}$ as a function of the detuning $\Delta_s = \omega_s - \omega_d/2$ for $\kappa = 500\gamma_m$ (solid curves) and $1000\gamma_m$ (dashed curves). We assumed that $\omega_m = \omega_d$ (resonant mechanical driving) in (a) and $\omega_m = 2\omega_s$ (resonant parametric coupling) in (b). For both plots, we assumed that $g_0 = 10\gamma_m$, $F = 50\gamma_m$, and $\sinh^2(r) = 0.5$.

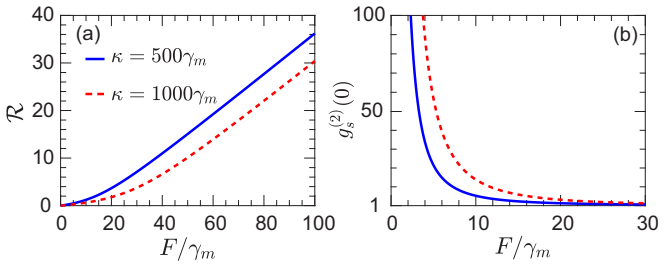

FIG. 15. (a) Signal-to-noise ratio $\mathcal{R}$ and (b) correlation function $g_s^{(2)}(0)$ versus the mechanical driving F for $\kappa = 500\gamma_m$ (solid curves) and $1000\gamma_m$ (dashed curves). For both plots, we assumed that $\omega_m = \omega_d = 2\omega_s$, $g_0 = 10\gamma_m$, and $\sinh^2(r) = 0.5$.

which is plotted as a function of the mechanical driving in Fig. 15(b). We find that $g_s^{(2)}(0)$ starts with very large values, and as the mechanical driving increases, $g_s^{(2)}(0)$ then decreases approaching 1. This behavior, as expected, suggests the phenomenon of photon bunching, thus confirming the DCE.

3. Analytical solutions in the limits $F \to 0$ and $F \to \infty$

In order to have a better analytical understanding, let us now consider the limit of $F \to 0$, and also the opposite limit of $F \to \infty$, at resonance $\omega_m = \omega_d = 2\omega_s$.

For the $F \to 0$ limit, we have $\langle a_s^\dagger a_s\rangle_{\rm ss} \to 0$, and thus, $x^n \approx 1 + 2n\langle a_s^\dagger a_s\rangle$ for $n = 0, 1, 2, \ldots$. Based on this, an approximate solution of the cubic equation in Eq. (C10) is found to be

$$\langle a_s^\dagger a_s\rangle_{\rm ss} \approx \frac{2g_{\rm DCE}^2}{\left(2g_{\rm DCE}^2+\gamma_0^2\right)^2}F^2, \quad \text{when} \quad F \to 0, \tag{C14}$$

which corresponds to Eq. (B13) for $n_{\rm th} = 0$. Analogously, we obtain

$$\left\langle a_s^2\right\rangle_{\rm ss} \approx -\frac{g_{\rm DCE}}{2g_{\rm DCE}^2+\gamma_0^2}F, \quad \text{when} \quad F \to 0, \tag{C15}$$

$$\langle b\rangle_{\rm ss} \approx -\frac{i\kappa}{2g_{\rm DCE}^2+\gamma_0^2}\frac{F}{2}, \quad \text{when} \quad F \to 0. \tag{C16}$$

Note that Eq. (C15) corresponds to Eq. (B14). Therefore, according to Eq. (B15), we obtain a quadratic increase in the ratio

$$\mathcal{R} = \frac{\Phi_{\rm DCE}}{\Phi_{\rm BGN}} \propto F, \tag{C17}$$

with large driving F, as shown in Fig. 15(a).

In the opposite limit of $F \to \infty$, we have $x \to 2\langle a_s^\dagger a_s\rangle_{\rm ss}$, and then obtain

$$\langle a_s^\dagger a_s\rangle_{\rm ss} \approx \frac{F}{2g_{\rm DCE}}, \quad \text{when} \quad F \to \infty, \tag{C18}$$

$$\left\langle a_s^2\right\rangle_{\rm ss} \approx -\frac{F}{2g_{\rm DCE}}, \quad \text{when} \quad F \to \infty, \tag{C19}$$

$$\left\langle b\right\rangle_{\rm ss} \approx -\frac{i\kappa}{4g_{\rm DCE}}, \quad \text{when} \quad F \to \infty. \tag{C20}$$

Consequently, the photon flux $\Phi_{\rm out}$ is given by

$$\Phi_{\rm DCE} = \frac{F}{2g_{\rm DCE}}\exp(2r), \quad \text{when} \quad F \to \infty. \tag{C21}$$

This indicates a linear increase in the ratio $\mathcal{R}$ with the driving F, as shown in Fig. 15(a).

For the $g_s^{(2)}(0)$ correlation in the limit of $F \to 0$, we find

$$g_s^{(2)}(0) \approx \frac{1}{2\langle a_s^\dagger a_s\rangle_{\rm ss}}, \quad \text{when} \quad F \to 0, \tag{C22}$$

which is the same as Eq. (B17). This corresponds to a large $g_s^{(2)}(0)$ as in Fig. 15(b) and, thus, to large photon bunching.

Furthermore, in the opposite limit of $F \to \infty$, the correlation function $g_s^{(2)}(0)$ is approximately equal to 1, i.e.,

$$g_s^{(2)}(0) \approx 1, \quad \text{when} \quad F \to \infty, \tag{C23}$$

as shown Fig. 15(b). This means that the DCE radiation field is approximately in a coherent state.

4. Stability analysis

We now turn to the multistability effects of our system. As discussed previously, in the semiclassical approximation, the system is governed by a cubic function. However, a cubic function has three solutions, and thus the system may exhibit multistability effects. To analyze them, we need to perform steady-state analysis [78]. Thus, we express the quantities $\langle a_s^\dagger a_s\rangle$, $\langle a_s^2\rangle$, and $\langle b\rangle$ as the sum of their steady-state values ($\langle a_s^\dagger a_s\rangle_{\rm ss}$, $\langle a_s^2\rangle_{\rm ss}$, $\langle b\rangle_{\rm ss}$) and time-dependent small perturbations [$\delta_1(t)$, $\delta_2(t)$, $\delta_3(t)$], that is,

$$\langle a_s^\dagger a_s\rangle = \langle a_s^\dagger a_s\rangle_{\rm ss} + \delta_1(t), \tag{C24}$$

$$\left\langle a_s^2\right\rangle = \left\langle a_s^2\right\rangle_{\rm ss} + \delta_2(t), \tag{C25}$$

$$\langle b\rangle = \langle b\rangle_{\rm ss} + \delta_3(t). \tag{C26}$$

Then, substituting these equations into Eqs. (C1)–(C3) yields

$$\begin{aligned}\frac{d}{dt}\delta_1(t) = i2g_{\rm DCE}\big(&\langle b\rangle_{\rm ss}^*\delta_2 + \left\langle a_s^2\right\rangle_{\rm ss}\delta_3^* \\ &- \langle b\rangle_{\rm ss}\delta_2^* - \left\langle a_s^2\right\rangle_{\rm ss}^*\delta_3\big) - \kappa\delta_1,\end{aligned} \tag{C27}$$

$$\begin{aligned}\frac{d}{dt}\delta_2(t) = &-i2\Delta_s\delta_2 - i2g_{\rm DCE}(2\langle a_s^\dagger a_s\rangle_{\rm ss}+1)\delta_3 \\ &- i4g_{\rm DCE}\delta_1\langle b\rangle_{\rm ss} - \kappa\delta_2,\end{aligned} \tag{C28}$$

$$\frac{d}{dt}\delta_3(t) = -i\Delta_m\delta_3 - ig_{\rm DCE}\delta_2 - \frac{\gamma_m}{2}\delta_3. \tag{C29}$$

We further make the following replacements:

$$\delta_1(t) \mapsto \exp(-i\omega t)x_1 + \exp(i\omega^* t)y_1^*, \tag{C30}$$

$$\delta_2(t) \mapsto \exp(-i\omega t)x_2 + \exp(i\omega^* t)y_2^*, \tag{C31}$$

$$\delta_3(t) \mapsto \exp(-i\omega t)x_3 + \exp(i\omega^* t)y_3^*, \tag{C32}$$

where x_k and y_k ($k = 1, 2, 3$) are time-independent complex numbers, and ω denotes a complex frequency. Then, the coupled equations (C27)–(C29) can be rewritten as

$$M\Psi = \omega\Psi, \tag{C33}$$

where

$$\Psi = (x_1, y_1, x_2, y_2, x_3, y_3)^T, \tag{C34}$$

$$M = i\begin{pmatrix} -\kappa & 0 & A^* & A & B^* & B \\ 0 & -\kappa & A^* & A & B^* & B \\ 2A & 0 & -i2\Delta_s-\kappa & 0 & C & 0 \\ 0 & 2A^* & 0 & i2\Delta_s-\kappa & 0 & C^* \\ 0 & 0 & -ig_{\rm DCE} & 0 & -i\Delta_m-\gamma_m/2 & 0 \\ 0 & 0 & 0 & ig_{\rm DCE} & 0 & i\Delta_m-\gamma_m/2 \end{pmatrix}, \tag{C35}$$

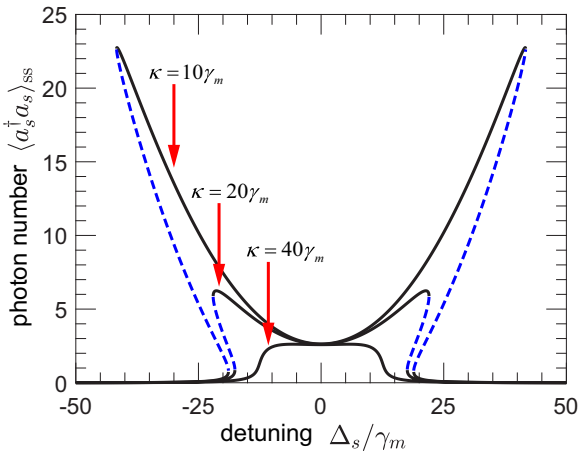

FIG. 16. Steady-state squeezed cavity mode photon number $\langle a_s^\dagger a_s \rangle_{ss}$ as a function of the detuning Δ_s for $\kappa = 10\gamma_m$, $20\gamma_m$, and $40\gamma_m$. Dashed curves represent unstable solutions. Here, we assumed that $\omega_m = 2\omega_s$, $g_0 = 10\gamma_m$, $F = 50\gamma_m$, and $\sinh^2(r) = 0.5$.

where

$$A = -i2g_{\rm DCE}\langle b\rangle_{ss}, \tag{C36}$$

$$B = i2g_{\rm DCE}\langle a_s^2\rangle_{ss}, \tag{C37}$$

$$C = -i2g_{\rm DCE}(2\langle a_s^\dagger a_s\rangle_{ss} + 1). \tag{C38}$$

If all imaginary parts of the eigenvalues of the matrix M are negative, then the system is stable; otherwise the system is unstable [79]. According to this criterion, we estimate the stability of our system. We find that for the parameters used in the above discussion about the DCE, the system does not exhibit multistability. Furthermore, when the mechanical loss is close to the cavity loss, we find for $\omega_m = 2\omega_s$ that the system becomes multistable, as shown in Fig. 16. However, the requirement that the mechanical loss is close to the cavity loss makes the threshold

$$F_{\rm th} = g_{\rm DCE} + \kappa\gamma_m/4g_{\rm DCE} \tag{C39}$$

very low. For $F \gg F_{\rm th}$, the system behaves classically, and quantum effects are negligible [55,56]. For the parameters in Fig. 16, the value of $F_{\rm th}$ is $\approx 9\gamma_m$ (here, we set $\kappa = 20\gamma_m$), which is smaller than one-fifth of the force $F = 50\gamma_m$. As a consequence, the system, when demonstrating such multistable behaviors, has probably reached the classical regime, where the DCE effect induced by the quantum fluctuations is negligible. Therefore, in order to observe the DCE, it is better to avoid the multistable regime of the system.

APPENDIX D: POSSIBLE IMPLEMENTATIONS WITH SUPERCONDUCTING QUANTUM CIRCUITS

Our scheme to implement the DCE is based on a generic optomechanical system, and at the same time, does not require an ultrahigh-frequency mechanical resonator and an ultrastrong single-photon coupling between light and mechanical motion. Therefore, we can expect that it can be implemented in various physical systems. In this section, as an example, we discuss in detail a possible implementation with superconducting circuits and, in particular, we refer to the experimental superconducting quantum circuit of Ref. [74], described by the standard optomechanical coupling of the form $a^\dagger a(b + b^\dagger)$.

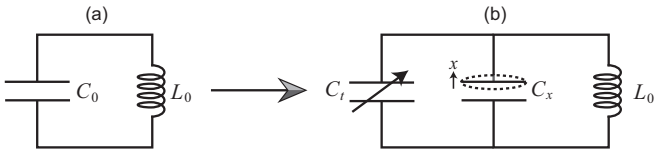

FIG. 17. (a) A standard LC circuit consisting of a capacitor (C_0) and an inductor (L_0). This circuit behaves as a single-mode microwave cavity. (b) An LC circuit used to implement the DCE. Its capacitor (C_x) is modulated by the mechanical motion, e.g., of a micromechanical membrane, and this results in a standard optomechanical coupling between light and mechanics. Meanwhile, the use of the electrically tunable capacitor (C_t) can parametrically drive and squeeze the cavity mode.

A standard LC circuit consists of a capacitor (e.g., with capacitance C_0) and an inductor (e.g., with inductance L_0), as shown in Fig. 17(a). Its Hamiltonian is expressed in terms of the capacitor charge Q and the inductor current I as

$$H_0 = \frac{\Phi^2}{2L_0} + \tfrac{1}{2}L_0\omega_0^2 Q^2, \tag{D1}$$

where $\Phi = L_0 I$ is the magnetic flux through the inductor, and $\omega_0 = 1/\sqrt{L_0 C_0}$ is the fundamental frequency of the circuit. After quantization, the charge Q and the flux Φ represent a pair of canonically conjugate variables, which obey the commutation relation $[Q, \Phi] = i\hbar$. Upon introducing a canonical transformation,

$$Q = \frac{1}{2}\sqrt{2\hbar\omega_0 C_0}(a + a^\dagger),$$
$$\Phi = \frac{1}{2i}\sqrt{2\hbar\omega_0 L_0}(a - a^\dagger), \tag{D2}$$

the Hamiltonian H_0 becomes

$$H_0 = \hbar\omega_0 a^\dagger a. \tag{D3}$$

Here, we have subtracted the constant zero-point energy $\hbar\omega_0/2$. Such an LC circuit thus behaves as a single-mode microwave cavity, with ω_0 being the cavity frequency, and with a ($a^\dagger$) being the annihilation (creation) operator of the cavity mode.

As demonstrated in Ref. [74], when the capacitance C_0 in Fig. 17(a) is modulated by the mechanical motion of a micromechanical membrane, the mechanical motion can couple to the cavity mode. In this manner, the capacitance C_0 becomes

$$C_0 \mapsto C_x = \frac{C_0}{1 + x/d}, \tag{D4}$$

where x is the displacement of the membrane, and d is the distance between the conductive plates of the capacitor. To parametrically squeeze the cavity mode, we further add an additional and electrically tunable capacitor into such an experimental setup. The LC circuit is shown in Fig. 17(b). Here, we assume the capacitance of the additional capacitor

to be

$$C_t = C_0 + \Delta C \cos(\omega_L t), \tag{D5}$$

where ω_L is the modulation frequency, and $\Delta C \ll C_0$. The total capacitance is thus given by $C_{\text{total}} = C_t + C_x$. Note that, in the absence of both mechanical motion and cosine modulation, the total capacitance is equal to $2C_0$, and as a result, the resonance frequency of the bare LC cavity, shown in Fig. 17(b), is $\omega_c = \omega_0/\sqrt{2}$, rather than $=\omega_0$. When both mechanical motion and cosine modulation are present, the cavity frequency ω_c is modulated as

$$\omega_c \mapsto \omega_c' = \frac{1}{\sqrt{L_0 C_{\text{total}}}} = \frac{\omega_0}{\sqrt{1 + \frac{\Delta C}{C_0}\cos(\omega_L t) + \frac{1}{1+x/d}}}. \tag{D6}$$

In the limit $\{\Delta C/C_0, x/d\} \ll 1$, we can expand ω_c', up to first order, to have

$$\omega_c' \approx \omega_c\left[1 - \frac{\Delta C}{4C_0}\cos(\omega_L t) + \frac{x}{4d}\right]. \tag{D7}$$

The Hamiltonian describing the cavity mode of the LC circuit in Fig. 17(b) is then given by

$$H_c = \frac{\Phi^2}{2L_0} + \frac{1}{2}L_0\omega_c^2\left[1 - \frac{\Delta C}{2C_0}\cos(\omega_L t) + \frac{x}{2d}\right]Q^2. \tag{D8}$$

Using the canonical transformation in Eq. (D2), but with ω_0 replaced by ω_c, the Hamiltonian H_c is reduced to

$$H_c = \hbar\omega_c a^\dagger a - \hbar g_0 a^\dagger a(b + b^\dagger) + \tfrac{1}{2}\hbar\Omega[\exp(i\omega_L t)a^2 + \exp(-i\omega_L t)a^{\dagger 2}], \tag{D9}$$

where b ($b^\dagger$) is the annihilation (creation) operator of the mechanical mode, $g_0 = -\omega_c x_{\text{zpf}}/4d$ is the single-photon optomechanical coupling, x_{zpf} is the zero-point fluctuation of the mechanical resonator, $\Omega = -\omega_c\Delta C/8C_0$ is the amplitude of the two-photon driving, and ω_L is its frequency. Here, we have made the rotating-wave approximation, and we have also replaced

$$x \mapsto x_{\text{zpf}}(b + b^\dagger). \tag{D10}$$

After including the free Hamiltonian of the mechanical resonator, the full Hamiltonian, in a rotating frame at $\omega_L/2$, becomes ($\hbar = 1$)

$$H = \omega_m b^\dagger b + \Delta a^\dagger a - g_0 a^\dagger a(b + b^\dagger) + \tfrac{1}{2}\Omega(a^2 + a^{\dagger 2}), \tag{D11}$$

where ω_m is the frequency of the mechanical mode, and $\Delta = \omega_c - \omega_L/2$. The Hamiltonian in Eq. (D11) is exactly the one applied by us in this work.

A squeezed-vacuum reservoir coupled to the cavity mode can be realized directly using the LC circuit in Fig. 17(a), but the constant capacitance C_0 needs to be replaced by a tunable capacitance C_t. By following the same recipe as above, the corresponding Hamiltonian is then given by

$$H_r = \Delta_0 a^\dagger a + \tfrac{1}{2}\Omega_0(a^2 + a^{\dagger 2}), \tag{D12}$$

where $\Delta_0 = \omega_0 - \omega_L/2$, and $\Omega_0 = -\omega_0\Delta C/8C_0$. The canonical transformation used here is the same as given in Eq. (D2). When the input field of the cavity is in the vacuum, we can obtain a squeezed-vacuum field at the output port, according to the input-output relation.

In addition to the LC circuit, the squeezed-vacuum reservoir can also be generated by a Josephson parametric amplifier, as experimentally demonstrated in Refs. [50,58]. In particular, a squeezing bandwidth of up to ∼10 MHz was reported in Ref. [50]. This is sufficient to fulfill the large-bandwidth requirement of the reservoir.

[1] J. Schwinger, On gauge invariance and vacuum polarization, Phys. Rev. **82**, 664 (1951).

[2] S. W. Hawking, Black hole explosions? Nature (London) **248**, 30 (1974).

[3] W. G. Unruh, Notes on black-hole evaporation, Phys. Rev. D **14**, 870 (1976).

[4] G. T. Moore, Quantum theory of the electromagnetic field in a variable-length one-dimensional cavity, J. Math. Phys. **11**, 2679 (1970).

[5] S. A. Fulling and P. C. W. Davies, Radiation from a moving mirror in two dimensional space-time: Conformal anomaly, Proc. R. Soc. London, Ser. A **348**, 393 (1976).

[6] V. V. Dodonov, Current status of the dynamical Casimir effect, Phys. Scr. **82**, 038105 (2010).

[7] P. D. Nation, J. R. Johansson, M. P. Blencowe, and F. Nori, *Colloquium:* Stimulating uncertainty: Amplifying the quantum vacuum with superconducting circuits, Rev. Mod. Phys. **84**, 1 (2012).

[8] E. Yablonovitch, Accelerating reference frame for electromagnetic waves in a rapidly growing plasma: Unruh-Davies-Fulling-Dewitt radiation and the nonadiabatic Casimir effect, Phys. Rev. Lett. **62**, 1742 (1989).

[9] Y. E. Lozovik, V. G. Tsvetus, and E. A. Vinogradov, Parametric excitation of vacuum by use of femtosecond laser pulses, Phys. Scr. **52**, 184 (1995).

[10] M. Crocce, D. A. R. Dalvit, F. C. Lombardo, and F. D. Mazzitelli, Model for resonant photon creation in a cavity with time-dependent conductivity, Phys. Rev. A **70**, 033811 (2004).

[11] C. Braggio, G. Bressi, G. Carugno, C. Del Noce, G. Galeazzi, A. Lombardi, A. Palmieri, G. Ruoso, and D. Zanello, A novel experimental approach for the detection of the dynamical Casimir effect, Europhys. Lett. **70**, 754 (2005).

[12] E. Segev, B. Abdo, O. Shtempluck, E. Buks, and B. Yurke, Prospects of employing superconducting stripline resonators for studying the dynamical Casimir effect experimentally, Phys. Lett. A **370**, 202 (2007).

[13] C. Ciuti, G. Bastard, and I. Carusotto, Quantum vacuum properties of the intersubband cavity polariton field, Phys. Rev. B **72**, 115303 (2005).

[14] S. De Liberato, C. Ciuti, and I. Carusotto, Quantum Vacuum Radiation Spectra from a Semiconductor Microcavity with a

Time-Modulated Vacuum Rabi Frequency, Phys. Rev. Lett. **98**, 103602 (2007).
[15] S. De Liberato, D. Gerace, I. Carusotto, and C. Ciuti, Extracavity quantum vacuum radiation from a single qubit, Phys. Rev. A **80**, 053810 (2009).
[16] L. Garziano, A. Ridolfo, R. Stassi, O. Di Stefano, and S. Savasta, Switching on and off of ultrastrong light-matter interaction: Photon statistics of quantum vacuum radiation, Phys. Rev. A **88**, 063829 (2013).
[17] D. Hagenmüller, All-optical dynamical Casimir effect in a three-dimensional terahertz photonic band gap, Phys. Rev. B **93**, 235309 (2016).
[18] S. De Liberato, Virtual photons in the ground state of a dissipative system, Nat. Commun. **8**, 1465 (2017).
[19] M. Cirio, K. Debnath, N. Lambert, and F. Nori, Amplified Optomechanical Transduction of Virtual Radiation Pressure, Phys. Rev. Lett. **119**, 053601 (2017).
[20] R. M. Souza, F. Impens, and P. A. M. Neto, Microscopic dynamical Casimir effect, Phys. Rev. A **97**, 032514 (2018).
[21] A. F. Kockum, A. Miranowicz, S. De Liberato, S. Savasta, and F. Nori, Ultrastrong coupling between light and matter, Nat. Rev. Phys. **1**, 19 (2019).
[22] P. Forn-Díaz, L. Lamata, E. Rico, J. Kono, and E. Solano, Ultrastrong coupling regimes of light-matter interaction, Rev. Mod. Phys. **91**, 025005 (2019).
[23] F. X. Dezael and A. Lambrecht, Analogue casimir radiation using an optical parametric oscillator, Europhys. Lett. **89**, 14001 (2010).
[24] J. R. Johansson, G. Johansson, C. M. Wilson, and F. Nori, Dynamical Casimir Effect in a Superconducting Coplanar Waveguide, Phys. Rev. Lett. **103**, 147003 (2009).
[25] J. R. Johansson, G. Johansson, C. M. Wilson, and F. Nori, Dynamical Casimir effect in superconducting microwave circuits, Phys. Rev. A **82**, 052509 (2010).
[26] C. M. Wilson, G. Johansson, A. Pourkabirian, M. Simoen, J. R. Johansson, T. Duty, F. Nori, and P. Delsing, Observation of the dynamical Casimir effect in a superconducting circuit, Nature (London) **479**, 376 (2011).
[27] D. A. R. Dalvit, Quantum physics: Shaking photons out of the vacuum, Nature (London) **479**, 303 (2011).
[28] J. R. Johansson, G. Johansson, C. M. Wilson, P. Delsing, and F. Nori, Nonclassical microwave radiation from the dynamical casimir effect, Phys. Rev. A **87**, 043804 (2013).
[29] P. Lähteenmäki, G. S. Paraoanu, J. Hassel, and P. J. Hakonen, Dynamical Casimir effect in a Josephson metamaterial, Proc. Natl. Acad. Sci. USA **110**, 4234 (2013).
[30] A. Lambrecht, M.-T. Jaekel, and S. Reynaud, Motion Induced Radiation from a Vibrating Cavity, Phys. Rev. Lett. **77**, 615 (1996).
[31] V. V. Dodonov and A. B. Klimov, Generation and detection of photons in a cavity with a resonantly oscillating boundary, Phys. Rev. A **53**, 2664 (1996).
[32] G. Plunien, R. Schützhold, and G. Soff, Dynamical Casimir Effect at Finite Temperature, Phys. Rev. Lett. **84**, 1882 (2000).
[33] G. Schaller, R. Schützhold, G. Plunien, and G. Soff, Dynamical Casimir effect in a leaky cavity at finite temperature, Phys. Rev. A **66**, 023812 (2002).
[34] W.-J. Kim, J. H. Brownell, and R. Onofrio, Detectability of Dissipative Motion in Quantum Vacuum via Superradiance, Phys. Rev. Lett. **96**, 200402 (2006).
[35] A. S. M. de Castro, A. Cacheffo, and V. V. Dodonov, Influence of the field-detector coupling strength on the dynamical Casimir effect, Phys. Rev. A **87**, 033809 (2013).
[36] V. Macrì, A. Ridolfo, O. Di Stefano, A. F. Kockum, F. Nori, and S. Savasta, Nonperturbative Dynamical Casimir Effect in Optomechanical Systems: Vacuum Casimir-Rabi Splittings, Phys. Rev. X **8**, 011031 (2018).
[37] M. Sanz, W. Wieczorek, S. Gröblacher, and E. Solano, Electromechanical Casimir effect, Quantum **2**, 91 (2018).
[38] H. Wang, M. P. Blencowe, C. M. Wilson, and A. J. Rimberg, Mechanically generating entangled photons from the vacuum: A microwave circuit-acoustic resonator analog of the oscillatory Unruh effect, Phys. Rev. A **99**, 053833 (2019).
[39] A. Settineri, V. Macrì, L. Garziano, O. Di Stefano, F. Nori, and S. Savasta, Conversion of mechanical noise into correlated photon pairs: Dynamical casimir effect from an incoherent mechanical drive, Phys. Rev. A **100**, 022501 (2019).
[40] M. O. Scully and M. S. Zubairy, *Quantum Optics* (Cambridge University Press, Cambridge, UK, 1997).
[41] Z. L. Xiang, S. Ashhab, J. Q. You, and F. Nori, Hybrid quantum circuits: Superconducting circuits interacting with other quantum systems, Rev. Mod. Phys. **85**, 623 (2013).
[42] X. Gu, A. F. Kockum, A. Miranowicz, Y.-x. Liu, and F. Nori, Microwave photonics with superconducting quantum circuits, Phys. Rep. **718-719**, 1 (2017).
[43] A. Reiserer and G. Rempe, Cavity-based quantum networks with single atoms and optical photons, Rev. Mod. Phys. **87**, 1379 (2015).
[44] X.-Y. Lü, Y. Wu, J. R. Johansson, H. Jing, J. Zhang, and F. Nori, Squeezed Optomechanics with Phase-Matched Amplification and Dissipation, Phys. Rev. Lett. **114**, 093602 (2015).
[45] M.-A. Lemonde, N. Didier, and A. A. Clerk, Enhanced nonlinear interactions in quantum optomechanics via mechanical amplification, Nat. Commun. **7**, 11338 (2016).
[46] W. Qin, A. Miranowicz, P.-B. Li, X.-Y. Lü, J. Q. You, and F. Nori, Exponentially Enhanced Light-Matter Interaction, Cooperativities, and Steady-State Entanglement Using Parametric Amplification, Phys. Rev. Lett. **120**, 093601 (2018).
[47] C. Leroux, L. C. G. Govia, and A. A. Clerk, Enhancing Cavity Quantum Electrodynamics via Antisqueezing: Synthetic Ultrastrong Coupling, Phys. Rev. Lett. **120**, 093602 (2018).
[48] C. K. Law, Interaction between a moving mirror and radiation pressure: A Hamiltonian formulation, Phys. Rev. A **51**, 2537 (1995).
[49] O. Di Stefano, A. Settineri, V. Macrì, A. Ridolfo, R. Stassi, A. F. Kockum, S. Savasta, and F. Nori, Interaction of Mechanical Oscillators Mediated by the Exchange of Virtual Photon Pairs, Phys. Rev. Lett. **122**, 030402 (2019).
[50] K. W. Murch, S. J. Weber, K. M. Beck, E. Ginossar, and I. Siddiqi, Reduction of the radiative decay of atomic coherence in squeezed vacuum, Nature (London) **499**, 62 (2013).
[51] M. Bartkowiak, L.-A. Wu, and A. Miranowicz, Quantum circuits for amplification of Kerr nonlinearity via quadrature squeezing, J. Phys. B **47**, 145501 (2014).
[52] J. B. Clark, F. Lecocq, R. W. Simmonds, J. Aumentado, and J. D. Teufel, Sideband cooling beyond the quantum backaction limit with squeezed light, Nature (London) **541**, 191 (2017).

[53] S. Zeytinoğlu, A. İmamoğlu, and S. Huber, Engineering Matter Interactions Using Squeezed Vacuum, Phys. Rev. X **7**, 021041 (2017).

[54] H. Vahlbruch, D. Wilken, M. Mehmet, and B. Willke, Laser Power Stabilization beyond the Shot Noise Limit Using Squeezed Light, Phys. Rev. Lett. **121**, 173601 (2018).

[55] C. M. Wilson, T. Duty, M. Sandberg, F. Persson, V. Shumeiko, and P. Delsing, Photon Generation in an Electromagnetic Cavity with a Time-Dependent Boundary, Phys. Rev. Lett. **105**, 233907 (2010).

[56] S. Butera and I. Carusotto, Mechanical backreaction effect of the dynamical casimir emission, Phys. Rev. A **99**, 053815 (2019).

[57] R. Stassi, A. Ridolfo, O. Di Stefano, M. J. Hartmann, and S. Savasta, Spontaneous Conversion from Virtual to Real Photons in the Ultrastrong-Coupling Regime, Phys. Rev. Lett. **110**, 243601 (2013).

[58] D. M. Toyli, A. W. Eddins, S. Boutin, S. Puri, D. Hover, V. Bolkhovsky, W. D. Oliver, A. Blais, and I. Siddiqi, Resonance Fluorescence from an Artificial Atom in Squeezed Vacuum, Phys. Rev. X **6**, 031004 (2016).

[59] T. J. Kippenberg, H. Rokhsari, T. Carmon, A. Scherer, and K. J. Vahala, Analysis of Radiation-Pressure Induced Mechanical Oscillation of an Optical Microcavity, Phys. Rev. Lett. **95**, 033901 (2005).

[60] A. Schliesser, P. Del'Haye, N. Nooshi, K. J. Vahala, and T. J. Kippenberg, Radiation Pressure Cooling of a Micromechanical Oscillator Using Dynamical Backaction, Phys. Rev. Lett. **97**, 243905 (2006).

[61] V. Fiore, Y. Yang, M. C. Kuzyk, R. Barbour, L. Tian, and H. Wang, Storing Optical Information as a Mechanical Excitation in a Silica Optomechanical Resonator, Phys. Rev. Lett. **107**, 133601 (2011).

[62] C. Dong, V. Fiore, M. C. Kuzyk, and H. Wang, Optomechanical dark mode, Science **338**, 1609 (2012).

[63] E. Verhagen, S. Deléglise, S. Weis, A. Schliesser, and T. J. Kippenberg, Quantum-coherent coupling of a mechanical oscillator to an optical cavity mode, Nature (London) **482**, 63 (2012).

[64] Z. Shen, Y.-L. Zhang, Y. Chen, C.-L. Zou, Y.-F. Xiao, X.-B. Zou, F.-W. Sun, G.-C. Guo, and C.-H. Dong, Experimental realization of optomechanically induced non-reciprocity, Nat. Photon. **10**, 657 (2016).

[65] F. Monifi, J. Zhang, Ş. K. Özdemir, B. Peng, Y.-x. Liu, F. Bo, F. Nori, and L. Yang, Optomechanically induced stochastic resonance and chaos transfer between optical fields, Nat. Photon. **10**, 399 (2016).

[66] J. U. Fürst, D. V. Strekalov, D. Elser, A. Aiello, U. L. Andersen, C. Marquardt, and G. Leuchs, Quantum Light from a Whispering-Gallery-Mode Disk Resonator, Phys. Rev. Lett. **106**, 113901 (2011).

[67] F. Sedlmeir, M. R. Foreman, U. Vogl, R. Zeltner, G. Schunk, D. V. Strekalov, C. Marquardt, G. Leuchs, and H. G. L. Schwefel, Polarization-Selective Out-Coupling of Whispering-Gallery Modes, Phys. Rev. Appl. **7**, 024029 (2017).

[68] L. S. Trainor, F. Sedlmeir, C. Peuntinger, and H. G. L. Schwefel, Selective Coupling Enhances Harmonic Generation of Whispering-Gallery Modes, Phys. Rev. Appl. **9**, 024007 (2018).

[69] S. Ast, M. Mehmet, and R. Schnabel, High-bandwidth squeezed light at 1550 nm from a compact monolithic PPKTP cavity, Opt. Express **21**, 13572 (2013).

[70] T. Serikawa, J. Yoshikawa, K. Makino, and A. Furusawa, Creation and measurement of broadband squeezed vacuum from a ring optical parametric oscillator, Opt. Express **24**, 28383 (2016).

[71] H. Vahlbruch, M. Mehmet, K. Danzmann, and R. Schnabel, Detection of 15 dB Squeezed States of Light and Their Application for the Absolute Calibration of Photoelectric Quantum Efficiency, Phys. Rev. Lett. **117**, 110801 (2016).

[72] R. Schnabel, Squeezed states of light and their applications in laser interferometers, Phys. Rep. **684**, 1 (2017).

[73] H. Flayac and V. Savona, Unconventional photon blockade, Phys. Rev. A **96**, 053810 (2017).

[74] J. D. Teufel, T. Donner, D. Li, J. W. Harlow, M. S. Allman, K. Cicak, A. J. Sirois, J. D. Whittaker, K. W. Lehnert, and R. W. Simmonds, Sideband cooling of micromechanical motion to the quantum ground state, Nature (London) **475**, 359 (2011).

[75] O. Gamel and D. F. V. James, Time-averaged quantum dynamics and the validity of the effective Hamiltonian model, Phys. Rev. A **82**, 052106 (2010).

[76] J. R. Johansson, P. D. Nation, and F. Nori, Qutip: An open-source Python framework for the dynamics of open quantum systems, Comput. Phys. Commun. **183**, 1760 (2012).

[77] J. R. Johansson, P. D. Nation, and F. Nori, Qutip 2: A Python framework for the dynamics of open quantum systems, Comput. Phys. Commun. **184**, 1234 (2013).

[78] D. Sarchi, I. Carusotto, M. Wouters, and V. Savona, Coherent dynamics and parametric instabilities of microcavity polaritons in double-well systems, Phys. Rev. B **77**, 125324 (2008).

[79] O. Kyriienko, T. C. H. Liew, and I. A. Shelykh, Optomechanics with Cavity Polaritons: Dissipative Coupling and Unconventional Bistability, Phys. Rev. Lett. **112**, 076402 (2014).